Department of Physics and Astronomy

University of Heidelberg

Master thesis

in Physics

submitted by

Valentin Titus Tenorth

born in Bottrop

2017

Consistent Models of Pseudoscalar Mediators for Dark Matter at the LHC

This Master thesis has been carried out by Valentin Titus Tenorth

at the

Institute for Theoretical Physics

under the supervision of

Prof. Dr. Tilman Plehn

Konsistente Modelle Pseudoskalarer Mediatoren für Dunkle Materie am LHC

In dieser Arbeit präsentieren wir ein Simplified Model für pseudoskalare Mediatoren, mit eichinvarianten Kopplungen an die Quarks des Standardmodells. Fermionische dunkle Materie wird mit Hilfe von effektiven Operatoren mit Massendimension fünf beschrieben, dies ermöglicht einen weiten Bereich möglicher Theorien für hohe Energien abzudecken.
Wir leiten gemeinsame Eigenschaften solcher Modelle her und die Parameter des erweiterten skalaren Sektors werden u. a. durch Ergebnisse aus der Higgs- und Flavorphysik, sowie direkter Suchen am LHC eingeschränkt. Der dunkle Materie Kandidat soll signifikant zur gesamten Menge dunkler Materie ausmachen und Ausschlussgrenzen von direkten und indirekten Suchen werden berücksichtigt. Ein besonderes Augenmerk liegt zudem auf der Suche nach mono-X Signalen am LHC.
Die experimentellen Ergebnisse aus verschiedenen Bereichen beschränken unseren Parameterraum stark. Ein realistischer Bereich bleibt auch in dem von uns gewählten minimalen Ansatz erhalten. Wir möchten betonen, dass resonante Zerfälle das mono-Z Signal in diesem Modell signifikant verstärken, was es notwendig macht, die Mediatoren für Suchen nach dunkle Materie am LHC explizit zu berücksichtigen. So führen die mono-Z Signale zu den stärksten Ausschlussgrenzen der mono-X Suchen und sind in der Lage beinahe den gesamten präferierten Parameterraum zu testen.

Consistent Models of Pseudoscalar Mediators for Dark Matter at the LHC

In this work we present a simplified model for a pseudoscalar dark matter mediator, embedded in a $SU(2)_L$ Higgs doublet, with gauge invariant couplings to Standard Model quarks. Effective couplings of dimension five to a fermionic dark matter candidate allow to cover a wide range of UV complete models.
Common properties of such models are derived and the parameter space is constrained from Higgs, flavor and collider physics. The dark matter candidate should contribute significantly to the relic abundance and is faced with results from direct as well as indirect detection experiments and searches for mono-X signals at the LHC.
The constraints cut into our parameter space from different directions, but still allow for a reasonable region in parameter space in our minimal approach without the need of additional states, which are likely to weaken the constraints. We emphasize that the resonantly enhanced production of mono-Z signals is able to test nearly the complete preferred parameter space, underlining the need of simplified models for dark matter searches at the LHC.

Contents

0 Introduction and Motivation

The story of dark matter started in the early 1930s with independent observations by the astronomers F. Zwicky and J. H. Oort. In 1932 Oort analyzed the vertical movement of stars in the Milky Way and found that there is not enough visible matter to bind the stars gravitationally. He proposed some additional amount of matter in the galactic center [1, 2]. One year later Zwicky was the first who called the amount of mass needed to explain the fact that the Coma cluster is gravitationally bound, “Dunkle Materie”. He probably thought of normal matter which was simply too cold and dark to be observed with the telescopes of these days [3]. From a present-day perspective this was the first evidence for dark matter.
Between 1939, again done by Oort, and the 1970’s by V. Rubin measurements of rotation velocities of galaxies over several length scales suggested a missing mass component. For a long time these observations have not been connected and remained an astronomical problem [4]. The rotation curves are still one of the most famous evidence for dark matter, although more convincing ones have been found in the last decades, e.g. in high precision measurements of the Cosmic Microwave Background (CMB), in simulations of cosmic structure formation, and in the observations of colliding galaxy clusters and gravitational lensing surveys [5, 6, 7, 8].
A consistent description of all these findings is obtained by dark matter, consisting of new particles, which are not described with the Standard Model of Particle Physics (SM). Therefore, dark matter is not just a problem of astrophysics or cosmology, but also of particle physics. It opens the door to new physics as it is one of the most stringent evidence for physics beyond the Standard Model. The search for the nature of dark matter is one of the major tasks of modern physics.

The range of explanations is extremely wide, e.g. the proposed masses of dark matter candidates reach from 10^{-22} eV[1], the bottom bound for bosonic dark matter, so called fuzzy dark matter [9], up to a few solar masses, assuming dark matter consists of primordial black holes [10]. In this work we concentrate on Weakly Interacting Massive Particles (WIMPs) with typical masses of a few GeV up to a few TeV. They represent one of the best motivated and probed dark matter candidates, because thermal production in the early Universe leads to the correct relic abundance as shown in Section 1.3. Even in this comparatively small mass range many different models and approaches to describe dark matter exist. The properties of the mediator of the interaction between the dark sector and Standard Model particles allow to distinguish between the different

[1]Throughout this work we will use natural units with $c = \hbar = k_B = 1$.

models. Possible mediators are scalar-, pseudoscalar-, vector-, and pseudovector-like bosons.
Experiments which search for dark matter can roughly be divided into three main strategies: direct detection, indirect detection and collider searches, which will be explained in more detail in the following chapter. Up to now no experiment found a convincing dark matter signal, but several constraints have been set on the properties of dark matter and the mediator. One should mention that there is no need for dark matter to interact with the Standard Model beyond gravitational interaction. In this case, it would be impossible to detect dark matter at a collider.
While models with scalar or vector mediators are strong constrained from direct detection experiments, collider experiments are particularly powerful in searching for pseudoscalar mediators.
Therefore, we want to investigate pseudoscalar mediators and derive universal signals for collider searches. We use a simplified model with explicit mediators embedded in an additional $SU(2)_L$ Higgs doublet and gauge invariant couplings to the Standard Model quarks. The couplings to dark matter are effective dimension five operators to cover a wide range of UV completions for the dark sector. Constraints from all three types search strategies for dark matter are taken into account here with a focus on mono-X signal searches at the Large Hadron Collider (LHC). In addition we want the dark matter candidate to contribute significantly to the relic abundance.

In the first chapter we give a short overview about the evidence, search strategies and candidates for dark matter and a first motivation for a consistent model for pseudoscalar mediators. The second chapter introduces general properties of so-called Two-Higgs-Doublet Models used in our approach. The specific model for pseudoscalar mediated dark matter is introduced and discussed in chapter three. In the fourth chapter constraints for the scalar and the dark sector from various experiments are discussed, especially mono-X searches at the LHC and relic density calculations. The last chapter will summarize the results and give a short conclusion and outlook.

1 General Aspects of Dark Matter

In this chapter we will shortly review some evidence for the existence and the particle nature of dark matter. After deriving the so-called WIMP miracle we will introduce the main search strategies for dark matter, briefly name some theoretical models, and motivate the model analyzed in this work.

1.1 Evidence for Dark Matter

In the last decades many evidence from astronomy, astrophysics, and cosmology for the existence of dark matter and its particle nature have been collected, some of them are discussed in the following. The structure of this chapter closely follows [2, 11].

1.1.1 Dynamics

The dynamics of astronomical objects at lenght scales varying from single galaxies to galaxy clusters give hints for the need of additional mass, which is provided by so far unknown and unseen "dark" matter. The general approach is to compare the amount of visible mass, estimated from stars, gas and dust clouds with the gravitational mass, which is derived from the observation that the systems are gravitationally bound.
In galaxies stars move on Kepler orbits around the center and their rotation velocity v at a distance r from the center follows from Newton's law

$$F_Z = F_g \qquad \Rightarrow \qquad \frac{v^2}{r} = \frac{GM(r)}{r^2} \qquad \Rightarrow \qquad v = \sqrt{\frac{GM(r)}{r}}\,. \tag{1.1}$$

Here $M(r) = 4\pi \int_0^r dr' r'^2 \rho(r')$ is the mass distribution of the galaxy, where ρ denotes the mass density by assuming a spherically symmetric system. The amount of visible matter is observed to be roughly constant over large radii in the outer regions. Therefore, decreasing rotation velocities are expected, but measurements show constant rotation velocities, even for distances of more than 10 kpc away from the galactic core. Figure 1.1 shows the measured rotation velocities in the galaxy NGC 6503 and curves calculated with the density profiles of the different galaxy constituents. It is obvious that the visible matter alone is not able to cause the measured velocities. A much better fit is obtained by adding a halo of dark matter around the galaxy.
Similar results at much bigger scales are obtained by observing orbital velocities in galaxy clusters, which are gravitationally bound systems of N orbiting objects. The

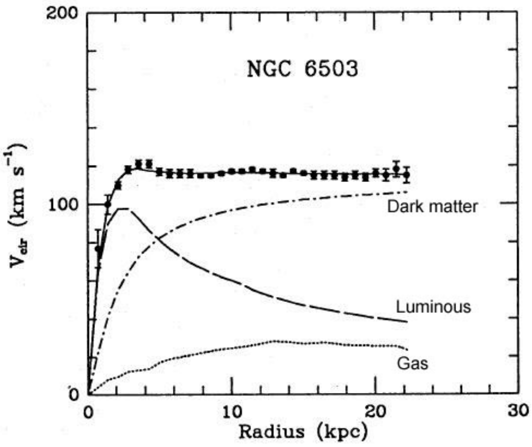

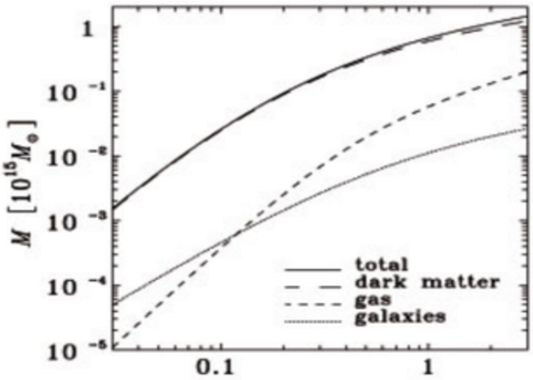

Figure 1.1: The left panel shows the rotation velocities of stars in the galaxy NGC 6503 depending on the distance from the center. Black dots denot the measured values. The lines for gas and luminous matter are calculated with the observed density profiles. The dark matter line is obtained by fitting the correct rotation velocities. Figure from [12].
On the right the amount of the three constituents and the total mass of the Coma cluster are shown within a relative radius r/r_{virial}. Over huge length scales dark matter clearly dominates. Figure from [13].

binding energy can be estimated as $U = -\frac{N(N-1)}{2}\frac{Gm^2}{r}$, where m and r are the average mass, and distance to the center of the cluster. Via the virial theorem the binding energy is related to the kinetic energy $T = \frac{Nmv^2}{2}$ and one gets

$$M = N\,m = \frac{2\,r\,v^2}{G}\,. \tag{1.2}$$

In 1933 Zwicky was the first who used the virial theorem to estimate the mass of a galaxy cluster from the orbital velocities. He found that the amount of visible mass is too low by a factor of ten to hold the galaxy cluster together. Actual measurements claim that the Coma cluster consists of roughly 85% dark matter, 14% hot intracluster medium (mainly hydrogen) and just 1% stars, their radial distributions are shown in the right panel of Figure 1.1 [13]. This indicates that dark matter is important for structures on cosmological length scales, too.

1.1.2 The Bullet Cluster

The observation of two colliding galaxy clusters is the most direct evidence of the particle nature of dark matter we have so far. The result excludes theories that try to explain the observed rotation curves with modifications of Newton's gravitational law

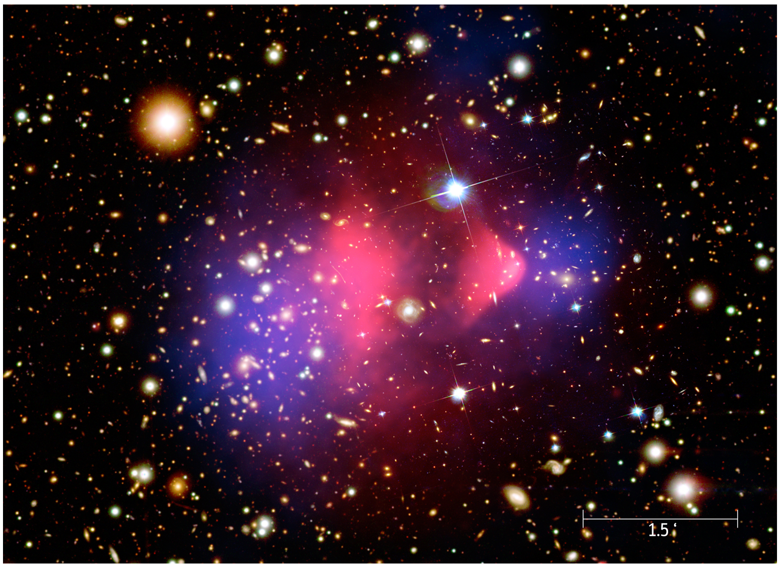

Figure 1.2: Collision of two galaxy clusters. The hot gas, observed via X-ray telescopes, carries most of the baryonic mass and is marked in red. The mass distribution measured via weak lensing is marked in blue and shows a significant separation from the baryonic mass. This strongly supports the existence of weakly interacting particle dark matter. Figure from [7].

or General Relativity, with a significance of 8σ, because dark and visible matter are clearly separated [7].

While one cluster - the right structure in Figure 1.2 - moved through the other one, the gas, which fills the space between the galaxies and carries most of the baryonic mass, collides, heats up and emits X-rays. Its shape takes the shape of the air around a bullet. On the other hand stars, galaxies and dark matter passed through each other with negligible interaction. X-ray measurements of the hot colliding gas indicate the position of the main amount of baryonic mass and weak gravitational lensing surveys the total mass distribution. The combination of both shows a significant separation of the visible mass and the strongest gravitational potential, see Figure 1.2 [7]. The strongest potential is found near the stars and galaxies and is caused by weakly interacting dark matter. As in this case, weak gravitational lensing surveys are a good method to map the matter distribution in various systems, especially for dark matter as it can not be observed with telescopes.

1.1.3 Cosmology

In 1964 A. Penzias and R. W. Wilson detected the CMB by chance. It was soon interpreted as the first direct evidence for the Big Bang theory.

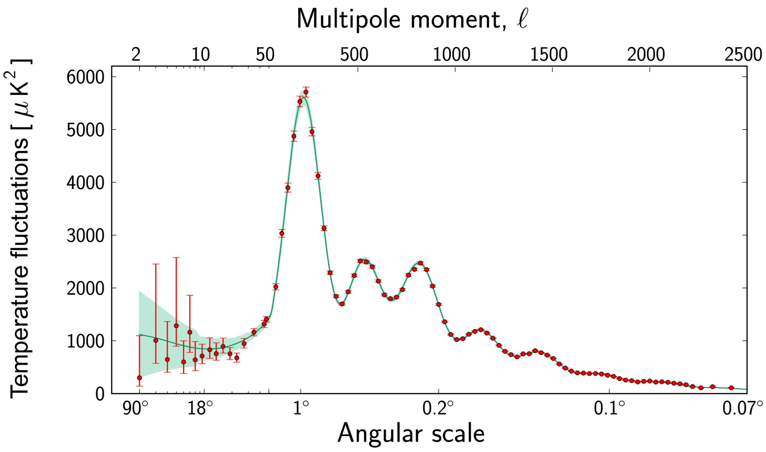

Figure 1.3: Power spectrum of the CMB temperature fluctuations measured by the Planck spacecraft in 2015. The dots denotes the measured values. Position and height of the peaks are determined by the amount of visible and dark matter. The line is a fit based on the ΛCDM-Model, which gives the values in Table 1.1. Figure from [14].

In the period of recombination[1], when the temperature of the universe dropped under roughly 3000 K or 0.3 eV, it was cold enough for nuclei to catch free electrons and form neutral atoms. Photons scattered no longer on free electrons and the universe became transparent. From this moment on the photons stream freely towards us and therefore are the oldest source of light, which is detectable today. Because of the expansion of the universe the relic photons are cooled down to roughly 2.7 K, which corresponds to a peak wavelength of approximately 160 GHz and gave rise to the name Cosmic Microwave Background.
A very precise mapping of the small temperature fluctuations ($\delta T/T < 10^{-5}$) in the CMB, was done by the Planck spacecraft. They are in good agreement with the Standard Model of cosmology, the ΛCDM-Model. This model assumes General Relativity and that our universe consists of Cold Dark Matter, a smaller fraction of baryonic matter and a cosmological constant Λ, also called dark energy. The temperature fluctuations are caused by anisotropies in the density of the primordial photon-baryon plasma. The fluctuations can be decomposed as a power spectrum of spherical harmonics, which define a basis for functions on the sphere. This power spectrum is shown in Figure 1.3 [14]. The measurements (dots) are in excellent agreement with the fit based on the ΛCDM-Model (line). Among other things the peaks positions and heights are used to determine the amount of visible and dark matter and the value of Λ, a more precise discussion for example can be found in [15]. The actual values are given in Table 1.1 and are the best measurements of the matter content in our universe we have so far. Every serious particle model for dark matter should reproduce this value.

[1] In the year $379,000$ after Big Bang. Also called time of last scattering or period of decoupling.

Type	Properties	$\Omega = \rho/\rho_{crit}$
Radiation	pressure	10^{-4}
Baryonic Matter	gravity and pressure	0.049 ± 0.0002
Dark Matter	only gravity	0.259 ± 0.002
Dark Energy	accelerates expansion	0.684 ± 0.009

Table 1.1: Relative contribution of the four constituents of the universe to the critical mass-energy density ρ_{crit} indicating a flat universe. Data from [15, 5].

Another argument for dark matter are actual computer simulations of large scale structure formation in the universe, like the Illustris-Project[2], which also largely confirm the ΛCDM-Model [6]. Those simulations deploy various astronomical observables and statistical quantities from the primordial density fluctuations derived from the CMB.
Their results are in good agreement with observations. For example the simulations of the Illustris-Project are able to reproduce all observed types of galaxies and the matter distribution on cosmological scales. Previous simulations, like the Aquarius Project, used only cold dark matter and got reasonable results for the cosmic structure. They show that the observed large scale structures in the universe need a high amount of cold dark matter, meaning non-relativistic, and exclud the existence of significant amounts of hot dark matter.

1.2 Candidates and other Explanations

In this work we consider particle dark matter, for completeness one should mention that there are other explanations on the market. Up to now, all evidence of dark matter comes from its gravitational effects, therefore a natural explanation would be to change our laws of gravity. An example are so-called MOND theories, which modify Newton's law and obtain very good results for fitting rotation curves of galaxies, but fail to explain other observations, like the Bullet Cluster [16]. In addition they are incompatible with General Relativity.
Generally speaking there are two ways to motivate new particles as dark matter candidates.
So far, all evidence for dark matter come from cosmology and astronomy, so it is reasonable to take the right cosmic abundance and a simple production mechanism, e.g. thermal production in the early universe to estimate the properties of such a particle without a full particle theory model. This is shown in the derivation of the so-called WIMP miracle below, which is the main motivation for this popular type of dark matter candidate. Here one has to derive a consistent model based on the properties of this particle.

[2]See http://www.illustris-project.org for images and further information.

A second approach is to consider proposed solutions to problems of the Standard Model, such as the strong CP or the hierachy problem, which could be solved by supersymmetric theories, or Axions, respectively. Many such theories imply new stable and neutral particles, which could be dark matter. On the other hand, any complete theory like the Minimal Supersymmetric Standard Model (MSSM) needs a reasonable dark matter candidate to be valid on its own. Among other things such a candidate has to be stable and neutral, because a charged and stable particle would have been observed [17]. The lightest supersymmetric particle (LSP) is stable because of an assumed R-parity conservation, which is also needed to forbid proton decays, and neutral, therefore it is dark matter candidate [18].

1.3 The WIMP Miracle - Relic Abundance with the Boltzmann Equation

Weakly Interacting Massive Particles (WIMPs) are one of the most preferred and natural candidates for Dark Matter. Since just a few and well motivated assumptions lead to the right cosmic abundance, it is called the WIMP miracle[3].

We assume that in the early universe one dark matter particle χ was in thermal equilibrium with the Standard Model particles f. The thermal equilibrium is maintained via some annihilation $f\bar{f} \leftrightarrow \chi\bar{\chi}$ with an interaction rate $\Gamma_\chi = n_\chi^2 \langle v\sigma \rangle$, where n_χ is the dark matter number density and $\langle v\sigma \rangle$ is the thermally averaged annihilation or interaction cross section. Thermal equilibrium requires that these interactions happen rapidly enough such that temperature fluctuations can be adjusted faster than the universe expanded, described by the time-depending Hubble function $H(t) = \frac{\dot{a}(t)}{a(t)}$, where $a(t)$ is the scale factor. The decoupling from the thermal bath (or freeze-out) happens when the interaction rate drops below the expansion rate of the universe $\Gamma_\chi < H(t)$.

A derivation of the WIMP miracle using this decoupling condition and some strong approximations can be found in [15, 4].

A more sophisticated derivation requires a solution of the Boltzmann equation in an expanding space. In general a Boltzmann equation quantifies the temporal change of a number density of a particle not in a thermal equilibrium. For $n_\chi(t)$ in the early universe it is given by

$$\dot{n}_\chi(t) \;=\; -3H(t)n_\chi(t) \;-\; \langle \sigma v \rangle \left(n_{\chi,EQ}^2(t) - n_\chi^2(t)\right), \tag{1.3}$$

where $n_{\chi,EQ}(t)$ is the corresponding equilibrium density, where the density drops only because of the expansion of the universe. Solving this equation is highly non-trivial and in general requires numerical methods. We use micrOmegas 4.3.1 to calculated the relic density in Chapter 4.7 [20, 21]. Nevertheless, with some approximations a quantitative result can be obtained analytically which is sketched in the following, more details can

[3] It should be mentioned, that the “WIMP miracle” is more of a possibility than a strong statement [19].

be found in e.g. [15, 22, 23, 4], and results from General Relativity and cosmology in e.g. [24].
First, Eq. (1.3) can be rewritten in terms of the temperature T using the thermodynamic relation $a(T)\,T \propto 1/g_{eff}(T) \approx$ const. [24]. This assumes that the number of effective degrees of freedom in the thermal bath g_{eff} stays constant. Therefore during the process of dark matter freeze-out the temperature change needs to be small, such that no other particle falls out of the thermal bath. g_{eff} is related to the number of Standard model particles with masses smaller than the temperature of the thermal bath. For $T > 175$ GeV all Standard Model particles are available and $g_{eff} = 106.75$, for $T = 5 - 80$ GeV the top quark and the weak gauge bosons are no longer active degrees of freedom, leading to $g_{eff} = 86.25$. The fractional numbers are caused by a different weight of bosonic and fermionic particles [15].
With this relation, and $H(t) = \frac{\dot{a}(t)}{a(t)}$, and defining a new quantity $Y(t) \equiv \frac{n(t)}{T^3}$, Eq. (1.3) reads

$$\frac{dY(t)}{dt} \;=\; -\,\langle\sigma v\rangle\; T^3(t)\left(Y^2(t) - Y_{eq}^2(t)\right)\,. \tag{1.4}$$

In a relativistic or radiation dominated universe the Hubble function fulfills the relations [15]

$$H(t) \;=\; \frac{1}{2t} \;=\; \sqrt{\frac{g_{eff}}{90}}\,\frac{\pi\,T^2(t)}{M_{Pl}} \;=\; \frac{H(x=1)}{x^2}\,, \tag{1.5}$$

where $M_{Pl} = 1/\sqrt{8\pi G} \approx 2.4 \times 10^{18}$ GeV is the reduced Planck mass. Using this expression the "rescaled inverse temperature" $x = m_\chi/T$, which is introduced as a new variable, can be written as

$$x = \sqrt{2tH(x=1)} \quad\rightarrow\quad \frac{dx}{dt} \;=\; \frac{H(x=1)}{x}\,. \tag{1.6}$$

Inserting this into Eq. (1.4) leads to [15]

$$\frac{dY(x)}{dx} \;=\; -\,\frac{\lambda(x)}{x^2}\,\left(Y^2(x) - Y_{eq}^2(x)\right)\,, \tag{1.7}$$

with

$$\lambda(x) \;=\; \sqrt{\frac{90}{g_{eff}}}\,\frac{M_{Pl}\,m_\chi}{\pi}\,\langle\sigma v\rangle\,(x)\,. \tag{1.8}$$

Two further assumptions are made to allow for an analytic solution. First, $Y_{eq}(x)$ is set to zero, because the equilibrium density of non-relativistic particles falls exponentially. Second, the thermally averaged annihilation cross section in Eq. (1.8) is expanded in terms of v and only the constant zeroth-order term is kept, therefore $\lambda(x)$ is roughly constant. With the ansatz $\bar{Y}(x) = 1/Y(x)$ the approximated Boltzmann equation can be solved to

$$\frac{1}{Y(x)} \;=\; -\frac{\lambda}{x} + \frac{1}{Y(x\to\infty)}\,. \tag{1.9}$$

Using the asymptotic behavior, one can replace $Y(x \to \infty) \equiv \frac{x_\infty}{\lambda(x_\infty)}$, where x_∞ is large enough to fulfill the boundary condition and greater than x_{dec}, the point of decoupling. As one now can calculate $Y(x \to \infty)$ (details in [15]), the density today $\rho_\chi(T_0) = m_\chi n_\chi(T_0)$ is obtained by rescaling the result at $x \to \infty$ using that any particle density drops with a^{-3} after decoupling because all distances in the Universe expand with a. Using again $a(T)T \propto 1/g_{eff}(T)$, the approximation $T_\infty \approx T_{dec}$, and $g_{eff}(T_{dec})/g_{eff}(T_0) = 28$ the density is given by

$$\rho_\chi(T_0) \;=\; m_\chi \left(\frac{a(T_\infty)T_\infty}{a(T_0)T_0}\right)^3 \frac{T_0^3}{T_\infty^3}\, n(T_\infty) \;=\; m_\chi \frac{T_0^3}{28}\, \frac{x_\infty}{\lambda(x_\infty)}\,. \tag{1.10}$$

To get a numerical value we again assume $\lambda(x)$ to be roughly constant and at the point of decoupling x_{dec} it is given by

$$\lambda(x_{dec}) \;\approx\; \sqrt{\frac{180}{x_{dec}\, g_{eff}(x_{dec})}}\, \frac{\alpha^2\, M_{Pl}\, m_\chi^3}{s_w\, M_W^4}\,. \tag{1.11}$$

In the previous step we assume an interaction mediated by the $W^\pm$ boson with mass $M_W \approx 80$ GeV, which gives a typical weak-scale cross section

$$\sigma_\chi \;=\; \frac{\pi\,\alpha^2\, m_\chi^2}{s_w^4 M_W^4}\,, \tag{1.12}$$

and non-relativistic velocities, therefore, $\frac{m_\chi v^2}{2} = T \;\leftrightarrow\; v = \sqrt{\frac{2T}{m_\chi}}$.
Typically the so-called relative energy-density $\Omega_\chi h^2 = \frac{\rho_\chi}{\rho_{crit}}$ is used to state the dark matter relic density, where $\rho_{crit} = 3H(t)^2 M_{Pl}^2$ is the critical density leading to a flat Universe and $h = 0.7$ is a ratio of the Hubble function used because of historical reasons. Now we can plug in all the numbers and compare the result to the Planck measurements in Table 1.1. We get

$$\Omega_\chi h^2 \;\approx\; 0.12\, \frac{x_{dec}}{28}\, \frac{\sqrt{g_{eff}}}{10} \left(\frac{50\ \text{GeV}}{m_\chi}\right)^2\,. \tag{1.13}$$

and with the first definition of $\lambda(x)$, we can express it in terms of the thermally averaged cross section

$$\begin{aligned} \Omega_\chi h^2 \;&=\; \sqrt{\frac{g_{eff}}{90}}\, \frac{x_{dec}}{28}\, \frac{h^2 \pi\, T_0^3}{3M_{Pl}^3\, H_0^3\, \langle\sigma v\rangle} \\ &\approx\; 0.12\, \frac{x_{dec}}{28}\, \frac{\sqrt{g_{eff}}}{10}\, \frac{10\ \text{fb}}{\langle\sigma v\rangle/c}\,. \end{aligned} \tag{1.14}$$

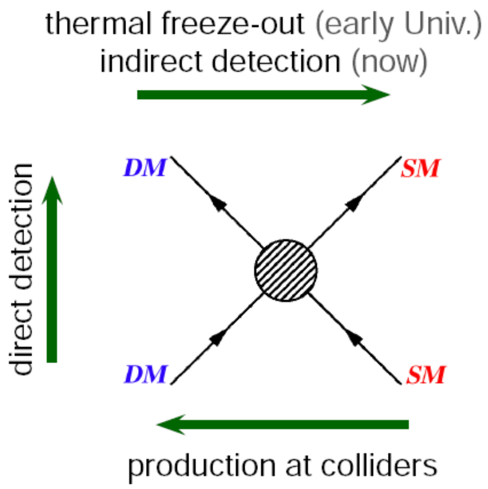

Figure 1.4: Sketch of the approaches to the Standard Model-dark matter interaction of the three main search strategies. Figure from [25].

Since $x_{dec} \approx 30$ and $g_{eff} = \mathcal{O}(100)$, as shown above, the derived equations are fulfilled by a particle with mass of $\mathcal{O}(100 \text{ GeV})$ and a thermally averaged cross section of $\mathcal{O}(10 \text{ fb})$. Again these are typical scales for a weakly interacting particle. If it was in thermal equilibrium after Big Bang, it was cold at the point of decoupling and leads to the right cosmic abundance $(\Omega_\chi h^2)^{Planck} \simeq 0.12$.

1.4 Search Strategies

There are three main ways to search for particle dark matter: indirect detection, direct detection and missing energy searches at particle colliders. They approach different aspects of the Standard Model-dark matter interaction, as sketched in Figure 1.4 [25]. Up to now none of it has detected a convincing dark matter signal. In the following, we will discuss these strategies and their sensitivity for testing different models for particle dark matter.

Indirect detection

Indirect detection experiments search for Standard Model remnants of dark matter annihilation processes or measure the effect of dark matter annihilation on other observables like the CMB or the lifetime of stars [17].
If somewhere in the universe two dark matter particles collide, they can annihilate to Standard Model particles, which then might be detected on earth. Examples are the IceCube experiment searching for neutrinos, the Alpha-Magnet-Spectrometer (AMS) located at the International Space Station (ISS) measuring charged cosmic rays like electrons and positrons, the Fermi Large Area Telescope and Imaging Air Cherenkov

Telescopes (IACT) such as H.E.S.S., VERITAS, MAGIC, and the new Cherenkov Telescope Array (CTA) searching for high energetic γ-rays from dark matter annihilation via Cherenkov radiation in the Earth's atmosphere [26].
Because the expected annihilation cross sections are small, the most promising regions are those with a high dark matter density, like the center of our galaxy. In these regions the background from astronomical processes is huge.
For these experiments the astrophysical backgrounds are complicated, so one looks for signals with low backgrounds, like antimatter or photon lines, and at places which might have a high dark matter density, such as the galactic center, (dark) dwarf galaxies or the sun. A main uncertainty come from the unknown dark matter distribution. Therefore the results are typically not as robust as the ones from direct detection and collider searches.
In contrast to this, the CMB is measured with very high precision and well understood. Dark matter annihilating to high energetic Standard Model states during the period of last scattering (redshift $z \approx 1000$) could modify the temperature and polarization of the CMB [27, 28].
We consider constraints on the total dark matter annihilation cross section, which are derived from CMB measurements and projectors of the CTA.

Direct detection

Direct detection experiments are low background experiments searching for only a few events per year. To obtain such low backgrounds the detectors are shielded against all kinds of radiation as good as possible and the remaining background is well understood, mostly originating from radioactive nuclei. For a further separation of signal and background events the annual modulation of the dark matter flux due to the motion of the Earth around the sun can be taken into account. These experiments, like XENON1T, which uses 3.2 t of liquid xenon as detector material, look for WIMPs with masses of a few GeV up to some TeV [29]. If a dark matter particle hits a xenon atom, it is ionized. The free electron as well as the light from recombination is detected. Lighter particles do not carry enough energy to create a measurable recoil, as dark matter has to be cold and therefore the kinetic energy is negligible.
Direct detection experiments nearly excluded WIMPs mediated by the electroweak bosons and those with scalar couplings to the nuclei, if they contribute significantly to the dark matter relic density. The bounds on the spin-independent WIMP-nucleon cross section from XENON1T are shown in Figure 1.5 [30].
For calculating the cross sections one can use effective field theories with four particle interactions because the momentum transfer is very small (in the keV range) compared to the typical mediator masses, e.g. 125 GeV for the Standard Model Higgs. Therefore, the mediator is never produced on-shell and the central condition for a valid EFT description $p \ll M_{Med}$ is fulfilled, where p is the transfered momentum and M_{Med} the mass of the mediator which is integrated out.

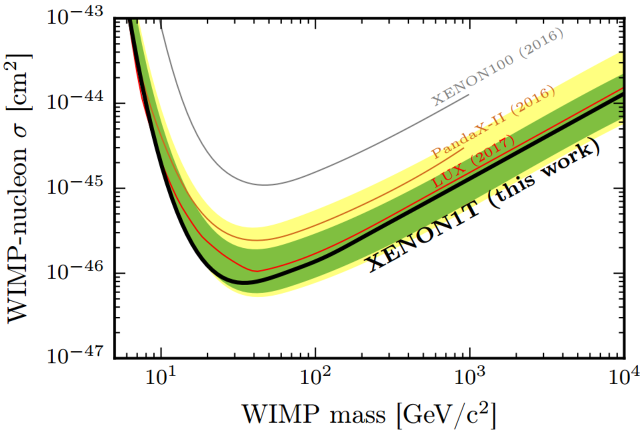

Figure 1.5: Exclusion limit for the spin-independent WIMP-nucleon interaction cross section for different WIMP masses from various experiments, especially from the new XENON1T experiment used in this work. Figure from [30].

Collider searches

Dark matter produced in high energy particle collisions leaves the detector without producing any signal and is searched by so-called mono-X events, where X can be a hadronic jet, a photon, a Z, $W^{\pm}$ or Higgs boson. The four momentum of all detected particles is summed up and large amounts of missing transverse momentum could indicate the production of dark matter, carrying the missing transverse energy. This is necessary as the total energy of collision at a proton collider is not known. A typical mono-X event would be a single high energetic jet, recoiled by invisible particle(s) like dark matter or neutrinos.

There are two ways to produce a mono-X signal: initial state radiation and resonant decays. The initial state radiation is dominated by jets and, therefore, mono-jet searches give the best results for a s-channel production of dark matter, as shown in Figure 1.6. In resonant decays the mediator is produced on-shell, which increases the cross section, and then decays to dark matter and Standard Model particles.

At the LHC the condition for a valid EFT approach is in general not fulfilled, as the momentum transfer is in the TeV range and mediators with masses around the weak scale can be produced on-shell, which leads to significantly enhanced event rates. Instead one has to use simplified models, which keep the mediator as a degree of freedom to cover this phenomenology, as shown in Figure 1.7 [32].

1.5 Possible Mediators and Implementations

We assume, that the dark sector contains at least one neutral particle with a mass compatible with the weak scale, and interacts with the Standard Model via some mediator.

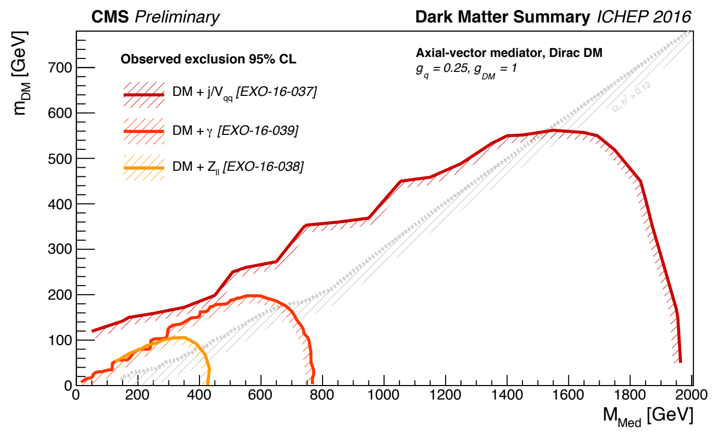

Figure 1.6: Comparison of exclusion limits obtained by different mono-X searches by the CMS experiment. For initial state radiation mono-jet gives the strongest bounds. Figure from [31].

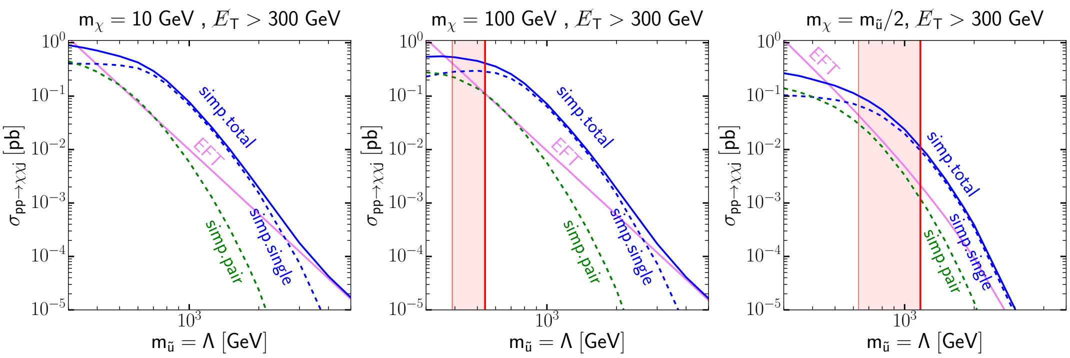

Figure 1.7: Examples for the mismatch of EFTs and simplified models for dark matter production cross section at the LHC. Figure from [32].

In the following possible mediators and their consequences for the different searches are discussed.
Dark matter mediated by the weak bosons or the Higgs are nearly excluded by direct detection searches. Therefore, one needs a mediator not included in the Standard Model. Possibilities are new spin 0 (scalars or pseudoscalars) or spin 1 particles, like a Z'. Effective Lagrangians for all mediators can e.g. be found in [33].
Spin 1 particles have to couple to the Standard Model quarks with a single gauge coupling to avoid Flavor Changing Neutral Currents (FCNC), which are strongly constrained from flavor observables. If the coupling is strong enough to produce a Z' at the LHC, it can decay back into quarks. Therefore, it is more promising to search for these mediators in die-jet or di-lepton final states.
Scalar mediators face strong constraints from direct detection experiments, which are stronger than bounds from collider searches. This is true as long as the dark matter particle is heavy enough to cause a measurable recoil, so for light WIMPs with masses below roughly 10 GeV, mono-X searches put stronger bounds on the cross section.
If instead the coupling is mediated by a pseudoscalar, the matrix element for scattering of Standard Model and dark matter particles scales like $v_\chi/c \ll 1$ [34], where $v_\chi \approx 200$ km/h is the mean dark matter velocity today. Therefore, there are no strong limits from direct detection and mono-X searches at colliders are the best possibility to test these mediators.
The Standard Model does not contain a pseudoscalar particle, but there are well motivated classes of theories, such as supersymmetric models, which are proposed to solve different problems within the Standard Model and enlarge the scalar sector such that it contains at least one pseudoscalar. To handle the high number of parameters of these full models, a good approach is to describe the phenomenology in simplified models, whereas additional states that are not relevant for the collider searches for dark matter are ignored. The simplest extension is one Standard Model singlet, with an effective coupling to quarks and a possible coupling to dark matter as both are singlets. Another way is to enlarge the Higgs sector by adding a second $SU(2)_L$ Higgs doublet, which contains a pseudoscalar and allows for gauge-invariant couplings to the Standard Model. Both approaches are shown in more detail in Chapter 3, where we concentrate on the second kind of model.

2 Two-Higgs-Doublet-Models

The consistent model presented and tested in the next chapters contains a second Higgs doublet and therefore it will be helpful to introduce the main implications of such an extended scalar part. A quite common modification of the Standard Model are the so-called two-Higgs-doublet models (2HDM), which introduce a second complex $SU(2)_L$ Higgs doublet. First, I give a short motivation for 2HDMs, second, the main properties of the extended scalar potential are shown, and third, couplings of the scalars needed in the following sections are derived.

2.1 Motivation

The ρ parameter, which is important to constrain theories beyond the Standard Model, for n scalar multiplets H_i with vacuum expectation value (vev) v_i, weak isospin I_i, and weak hypercharge Y_i is at tree level given by

$$\rho = \frac{\sum_{i=1}^{n}\left[I_i(I_i+1)-\frac{1}{4}Y_i^2\right]v_i}{\sum_{i=1}^{n}\frac{1}{2}Y_i^2 v_i} \overset{exper.}{=} 1.00037 \pm 0.00023\,, \tag{2.1}$$

where the experimental value shows only $1.6\,\sigma$ deviation from the Standard Model expectation of 1 [35]. As a result $SU(2)_L$ singlets with $Y = 0$ and $SU(2)_L$ doublets with $Y = \pm 1$ and $I(I+1) = \frac{3}{4}Y^2$ are preferred as they keep $\rho = 1$.

The Higgs mechanism for electroweak symmetry breaking realized in the Standard Model is the "most economic version", but there is no reason that there are no additional scalars. As a simple analogy to the three generations of fermions one could assume that there is more than one scalar in nature. In addition 2HDMs could provide additional phase transitions in the early Universe, which are needed to explain the baryon asymmetry. In supersymmetric theories like the MSSM a second Higgs doublet is required, to generate masses via the Higgs mechanism.

2.2 Particle Content

The two doublets can be written in different bases, for example in the interaction-base as

$$H_i = \begin{pmatrix} \phi_i^+ \\ (v_i+\rho_i+i\eta_i)/\sqrt{2} \end{pmatrix} \qquad \text{with } i = 1,2\,. \tag{2.2}$$

Both doublets can acquire vevs v_i, which had to fulfill the relation $\sqrt{v_1^2 + v_2^2} = v = 246$ GeV and we define $\tan(\beta) = t_\beta = \frac{v_2}{v_1}$.
The two doublets contain eight scalar fields. Three of them correspond to the massless Standard Model Goldstone bosons G_0 and $G^\pm$, which are eaten by the $SU(2)_L$ gauge bosons $W^\pm$ and Z and give them their masses. The remaining five are physical scalars or Higgs fields. There are two charged scalars $H^\pm$, two neutral scalars h and H, where h usually denotes the lighter one, and a pseudoscalar A.
The rotation to diagonalize the mass-matrices and get the mass eigenstates for the neutral scalars is given by

$$\begin{pmatrix} h \\ H \end{pmatrix} = \begin{pmatrix} s_\alpha & -c_\alpha \\ -c_\alpha & -s_\alpha \end{pmatrix} \begin{pmatrix} \rho_1 \\ \rho_2 \end{pmatrix} , \tag{2.3}$$

with $s_\alpha \equiv \sin(\alpha),\ c_\alpha \equiv \cos(\alpha)$ and for the charged scalars by

$$\begin{pmatrix} G^\pm \\ H^\pm \end{pmatrix} = \begin{pmatrix} c_\beta & s_\beta \\ -s_\beta & c_\beta \end{pmatrix} \begin{pmatrix} \phi_1^\pm \\ \phi_2^\pm \end{pmatrix} , \tag{2.4}$$

and the pseudoscalars

$$\begin{pmatrix} G^0 \\ A \end{pmatrix} = \begin{pmatrix} c_\beta & s_\beta \\ s_\beta & -c_\beta \end{pmatrix} \begin{pmatrix} \eta_1 \\ \eta_1 \end{pmatrix} . \tag{2.5}$$

In this discussion we use this rotations to express the doublets H_i in the mass eigenstates, where [36]

$$H_1 = \frac{1}{\sqrt{2}} \begin{pmatrix} \sqrt{2}\,(c_\beta G^+ - s_\beta H^+) \\ v_1 + c_\alpha H - s_\alpha h + i(c_\beta G_0 - s_\beta A) \end{pmatrix} , \tag{2.6}$$

$$H_2 = \frac{1}{\sqrt{2}} \begin{pmatrix} \sqrt{2}\,(s_\beta G^+ + c_\beta H^+) \\ v_2 + s_\alpha H + c_\alpha h + i(s_\beta G_0 + c_\beta A) \end{pmatrix} . \tag{2.7}$$

The scalar corresponding to the Standard Model Higgs boson can be expressed in terms of the 2HD interaction or mass eigenstates by

$$h^{SM} = \rho_1\, c_\beta + \rho_2\, s_\beta = s_{\beta-\alpha}\, h - c_{\beta-\alpha}\, H . \tag{2.8}$$

Since the ATLAS and CMS experiments at the LHC discovered a Standard Model Higgs like scalar with a mass of 125 GeV, we want the light scalar h to have the measured properties and behave like the Standard Model Higgs boson[1]. This can be achieved in the so called alignment limit, where $c_{\beta-\alpha} = 0$, or the decoupling limit, where the other spin 0 particles are heavy, this forces $c_{\beta-\alpha} \to 0$ again [38].

[1]It is possible to choose H as the measured scalar but the constraints are much harder and complicated [37]

2.3 The Scalar Potential

The product of a $SU(2)_L$ doublet and its hermitian conjugate forms a Standard Model singlet, which means that it is invariant under all Standard Model gauge groups. Therefore they, can be combined in many ways to form the general potential

$$\begin{aligned} V_{2HD}^{gen} =\; & \mu_1 H_1^\dagger H_1 + \mu_2 H_2^\dagger H_2 + \left[\mu_3 H_1^\dagger H_2 + h.c.\right] + \lambda_1 \left(H_1^\dagger H_1\right)^2 + \lambda_2 \left(H_2^\dagger H_2\right)^2 \\ & + \lambda_3 \left(H_1^\dagger H_1\right)\left(H_2^\dagger H_2\right) + \lambda_4 \left(H_1^\dagger H_2\right)\left(H_2^\dagger H_1\right) + \left[\lambda_5 \left(H_1^\dagger H_2\right)^2 \right. \\ & \left. + \lambda_6 \left(H_1^\dagger H_1\right)\left(H_1^\dagger H_2\right) + \lambda_7 \left(H_2^\dagger H_2\right)\left(H_1^\dagger H_2\right) + h.c.\right], \end{aligned} \tag{2.9}$$

where the parameters μ_3 and $\lambda_{5,6,7}$ are complex. These 14 degrees of freedom are reduced to 11 physical parameters because of the freedom to redefine the basis.
Applying symmetries reduces the number of degrees of freedom. In this work CP conservation and a new global symmetry under which $H_1^\dagger H_2$ is charged are assumed. Applying this symmetries to the most general 2HD potential from Eq. (2.9) leads to

$$\begin{aligned} V_{2HD} =\; & \mu_1 H_1^\dagger H_1 + \mu_2 H_2^\dagger H_2 + \left(\mu_3 H_1^\dagger H_2 + h.c.\right) + \lambda_1 \left(H_1^\dagger H_1\right)^2 \\ & + \lambda_2 \left(H_2^\dagger H_2\right)^2 + \lambda_3 \left(H_1^\dagger H_1\right)\left(H_2^\dagger H_2\right) + \lambda_4 \left(H_1^\dagger H_2\right)\left(H_2^\dagger H_1\right) , \end{aligned} \tag{2.10}$$

where all coefficients are real, especially μ_3 is chosen to be real to avoid CP violating mixing of the scalars and the pseudoscalar. We allow for a soft breaking of the new symmetry by operators with mass dimension smaller than four, such that $\mu_3 H_1^\dagger H_2 + h.c.$ is allowed and generates a mass term for the pseudoscalar A. This is necessary because massless pseudoscalars are excluded by experiments.
The number of parameters is reduced to seven, with three of them μ_1, μ_2, μ_3 having mass dimension two and four of them λ_1, λ_2, λ_3, λ_4 having mass dimension zero.
A basic requirement for any meaningful physical theory is the existence of a stable minimum, here it means that the scalar potential is bounded from below. Therefore, no direction in field space exists where $V_{2HD} \to -\infty$. This can be achieved by the "strong stability" requirement, where $V_{2HD} > 0$ for all $H_i \to \infty$.
Necessary conditions are obtained by investigating the behavior in different directions of field space, e.g. from $|H_1| \to \infty$ and $|H_2| = 0$ follows $\lambda_1 \geq 0$. Testing different cases imposes the conditions [39]

$$\lambda_1 > 0\,, \qquad \lambda_2 > 0\,, \qquad \lambda_3 > -\sqrt{\lambda_1 \lambda_2}\,, \qquad \lambda_4 + \lambda_3 + \sqrt{\lambda_1 \lambda_2} > 0\,, \tag{2.11}$$

which are proven to be sufficient, if $\lambda_5 = \lambda_6 = \lambda_7 = 0$, as in our case [40, 41].
The requirement of perturbativity of the dimensionless couplings requires

$$\lambda_i < 4\pi \qquad \text{with } i = 1, 2, 3, 4\,. \tag{2.12}$$

The potential coefficients can be traded for the physical input parameters we use in our analyses: the vacuum expectation values of the two Higgs doublets v_1 and v_2 or $v = 246$ GeV and $t_\beta = v_1/v_2$, the masses of the physical scalars $m_h = 125$ GeV, $M_H, M_{H^\pm}$, and of the pseudoscalar M_A, and the scalar mixing angle $c_{\beta-\alpha}$ (or $s_{\beta-\alpha}$). The potential coefficients are given by [36]

$$\mu_1 = s_\beta^2 M_A^2 - \frac{c_{\beta-\alpha}\, c_\alpha M_H^2 - s_{\beta-\alpha}\, s_\alpha M_h^2}{2\, c_\beta}, \tag{2.13}$$

$$\mu_2 = c_\beta^2 M_A^2 - \frac{c_{\beta-\alpha}\, s_\alpha M_H^2 + c_\alpha\, s_{\beta-\alpha} M_h^2}{2\, s_\beta}, \tag{2.14}$$

$$\mu_3 = s_\beta\, c_\beta\, M_A^2, \tag{2.15}$$

$$\lambda_1 = \frac{c_\alpha^2 M_H^2 + s_\alpha^2 M_h^2 - s_\beta^2 M_A^2}{2\, v^2\, c_\beta^2}, \tag{2.16}$$

$$\lambda_2 = \frac{s_\alpha^2 M_H^2 + c_\alpha^2 M_h^2 - c_\beta^2 M_A^2}{2\, v^2\, s_\beta^2}, \tag{2.17}$$

$$\lambda_3 = \frac{s_\alpha\, c_\alpha\, (M_H^2 - M_h^2) + s_\beta\, c_\beta \left(2M_{H^\pm}^2 - M_A^2\right)}{v^2\, c_\beta\, s_\beta}, \tag{2.18}$$

$$\lambda_4 = \frac{2\left(M_A^2 - M_{H^\pm}^2\right)}{v^2}. \tag{2.19}$$

For completeness we also show the relations between the Higgs masses and the potential-coefficients

$$m_h^2 = \frac{c_{\beta-\alpha}^2\, \mu_3}{c_\beta\, s_\beta} + 2\, v^2 \left(\lambda_1 c_\beta^2 s_\alpha^2 + \lambda_2 s_\beta^2 c_\alpha^2 - (\lambda_3 + \lambda_4) c_\beta c_\alpha s_\beta s_\alpha\right), \tag{2.20}$$

$$M_H^2 = \frac{s_{\beta-\alpha}^2\, \mu_3}{c_\beta\, s_\beta} + 2\, v^2 \left(\lambda_1 c_\beta^2 c_\alpha^2 + \lambda_2 s_\beta^2 s_\alpha^2 + (\lambda_3 + \lambda_4) c_\beta c_\alpha s_\beta s_\alpha\right), \tag{2.21}$$

$$M_A^2 = \frac{\mu_3}{c_\beta\, s_\beta}, \tag{2.22}$$

$$M_{H^\pm}^2 = \frac{\mu_3}{c_\beta\, s_\beta} - \frac{\lambda_4\, v^2}{2}. \tag{2.23}$$

2.4 Yukawa Couplings

Now we want to look at the Yukawa part of 2HDMs. In general both doublets could couple to fermions. But both coupling matrices are not necessarily diagonalized by the mass eigenstates. This leads to strong flavor changing neutral currents which are nearly excluded by flavor experiments. To avoid this one usually assumes an additional Z_2 symmetry with charges such that one doublet couples to one type of fermions. With

2HDM	H_u	H_d	H_l
Type I	H_1	$\tilde{H}_1$	$\tilde{H}_1$
Type II	H_1	H_2	H_2
Type X	H_1	$\tilde{H}_1$	$\tilde{H}_2$
Type Y	H_1	$\tilde{H}_2$	$\tilde{H}_1$

Table 2.1: Assignment of the two Higgs doublets to the states in Eq. (2.24) for different types of 2HDMs. Naming of the types follow [42].

such a symmetry the Yukawa Lagrangian reads as

$$\mathcal{L}_{Yuk} \;=\; \sum_{i,j=1}^{3} y_{ij}^{u}\bar{Q}_i\,\tilde{H}_u\,u_j \;+\sum_{i,j=1}^{3} y_{ij}^{d}\bar{Q}_i\,H_d\,d_j \;+\sum_{i,j=1}^{3} y_{ij}^{\ell}\bar{L}_i\,H_l\,\ell_j \;+\; h.c.\,, \tag{2.24}$$

where H_u, H_d and H_l are either H_1 or H_2, depending on the chosen type of 2HDM, see Table 2.1. This work is restricted to models with natural flavor conservation and 2HDMs of type I and II.
After electroweak symmetry breaking, and choosing the mass eigenstate basis, the Yukawa Lagrangian can be written as

$$\begin{aligned}\mathcal{L}_{Yuk} \;=& \sum_{f=u,d,l} \big(g_{hf}\bar{f}fh + g_{Hf}\bar{f}fH - ig_{Af}\bar{f}\gamma_5 fA\big) - \frac{\sqrt{2}}{v}\,H^+\times \\ &\left(\sum_{i,j=1}^{3}\big(\bar{u}_iV_{ij}\left(\kappa_{H^+d}m_{d_j}P_R - \kappa_{H^+u}m_{u_i}P_L\right)d_j + \kappa_{H^+\ell}\bar{\nu}m_\ell P_R\ell\big) + h.c.\right)\,.\end{aligned} \tag{2.25}$$

Couplings between Standard Model fermions f and the neutral scalars $\varphi = h, H, A$ can be written as $g_{\varphi f} = \kappa_{\varphi f}\, g_{hf}^{\mathrm{SM}}$, in which $g_{hf}^{\mathrm{SM}} = m_f/v$ are the respective Standard Model Higgs couplings. The values for $\kappa_{\varphi f}$ depend on the chosen type of 2HDM and are given in Table 2.2. The couplings of the charged Higgs to the Standard Model fermions are given in the second line of Eq. (3.15) with $\kappa_{H^+f} = \kappa_{Af}$ for all fermions f, and V_{ij} as the elements of the CKM matrix, and $P_{L/R}$ as projection operators for left-/right-handed fermions.

Type I	Type II	
$\kappa_{hu} = \kappa_{hd} = \kappa_{h\ell} = s_{\beta-\alpha} + \frac{c_{\beta-\alpha}}{t_\beta}$	$\kappa_{hu} = s_{\beta-\alpha} + \frac{c_{\beta-\alpha}}{t_\beta}$,	$\kappa_{hd} = \kappa_{h\ell} = -s_{\beta-\alpha} - c_{\beta-\alpha}\, t_\beta$
$\kappa_{Hu} = \kappa_{Hd} = \kappa_{H\ell} = c_{\beta-\alpha} - \frac{s_{\beta-\alpha}}{t_\beta}$	$\kappa_{Hu} = c_{\beta-\alpha} - \frac{s_{\beta-\alpha}}{t_\beta}$,	$\kappa_{Hd} = \kappa_{H\ell} = c_{\beta-\alpha} + s_{\beta-\alpha}\, t_\beta$
$\kappa_{Au} = \kappa_{Ad} = \kappa_{A\ell} = -\frac{1}{t_\beta}$	$\kappa_{Au} = -\frac{1}{t_\beta}$,	$\kappa_{Ad} = \kappa_{A\ell} = t_\beta$

Table 2.2: Modifications of the Standard Model Yukawa couplings by $\kappa_{\phi f}$ for the scalars and the pseudoscalar in 2HDMs of type I and II [42].

3 The Simplified Model

In this chapter we introduce the Lagrangian of the consistent simplified model discussed in this work as well as possible UV-completions. Then we derive important properties of this model and discuss the branching ratios of the scalars.

3.1 The Lagrangian

As motivated in the introduction, we want to investigate common structures of models with a pseudoscalar mediator for dark matter, which are valid for wide range of possible UV completions.
Because there is no pseudoscalar particle in the Standard Model, one has to add such a particle in a consistent way and there are at least two ways to do this. In addition, we take a Standard Model singlet Dirac fermion χ as the dark matter candidate.
The simplest extension is a pseudoscalar singlet a, which has effective couplings of dimension five to the Standard Model quarks and a renormalizable dark matter coupling as both are singlets,

$$\mathcal{L} \,=\sum_{i,j=1}^{3} y_{ij}^{q}\,\frac{a}{\Lambda}\,\bar{Q}_i\,\gamma_5\,q_j\,H \,+\, \sum_{i,j=1}^{3} y_{ij}^{\ell}\,\frac{a}{\Lambda}\,\bar{L}_i\,\gamma_5\,\ell_j\,H \,+\, c_s\,a\,\bar{\chi}\gamma_5\chi \,+\, h.c.\,, \tag{3.1}$$

where Λ is the scale of new heavy physics and typically in the TeV range. Models of this type face several problems in collider searches. First, the production of a via gluon fusion is suppressed with respect to the Standard Model Higgs production by a factor v/Λ. Second, in such a model only initial state radiation is possible, which does not lead to model specific phenomenology.
The second class of models is obtained by embedding the pseudoscalar in a second $SU(2)_L$ Higgs doublet. This allows for a gauge invariant coupling of dimension four of the pseudoscalar to the Standard Model fermions, therefore, the production cross section is not suppressed. We use effective couplings to dark matter to be as general as possible, which are suppressed with factor v/Λ compared with the couplings to Standard Model fermions, but dark matter still dominates the branching ratio of the pseudoscalar as the competing coupling to b-quarks is rather small. The additional scalar degrees of freedom are kept to cover aspects of the phenomenology of UV completions

and to ensure the validity of the EFT approach, see Figure 1.7, leading to

$$
\begin{aligned}
\mathcal{L} \;=&\; \sum_{i,j=1}^{3} y_{ij}^{u}\, \bar{Q}_i\, H_1\, u_j \,+\, \sum_{i,j=1}^{3} y_{ij}^{d}\, \bar{Q}_i\, H_2\, d_j \,+\, \sum_{i,j=1}^{3} y_{ij}^{\ell}\, \bar{L}_i\, H_2\, \ell_j \\
&+\, c_\chi\, \frac{H_1^\dagger H_2}{\Lambda}\, \bar{\chi}\chi \,+\, c_5\, \frac{H_1^\dagger H_2}{\Lambda}\, \bar{\chi}\gamma_5\chi \,+\, m_\chi\, \bar{\chi}\chi \,+\, h.c.\,,
\end{aligned} \tag{3.2}
$$

where we also consider an explicit mass term for the dark matter candidate. Here, the Yukawa couplings of a 2HDM of type II are chosen, but we also consider a 2HDM of type I, obtained by the replacements in Table 2.1.
To reduce the number of terms the, symmetry, assumed in the previous chapter to simplify the scalar potential in Eq. (2.10), is extended such that the Standard Model singlets $H_1^\dagger H_2$, $\bar{\chi}\chi$ and $\bar{\chi}\gamma_5\chi$ carry a charge. Again the symmetry is softly broken by the explicit dark matter mass term. This kind of symmetry can also be motivated from flavor physics as it could serve as an explanation for the huge hierarchy in the Yukawa couplings [43]. The discussion of the flavor implications of this symmetry is very interesting as the additional dark matter couplings, presented here, might relax the strong flavor constraints, and planned to be discussed in a following work.
Theoretical aspects and the phenomenology of this model are discussed in the following. The effective dark matter couplings in Eq. (3.2) can be obtained from several well-motivated UV completions, by considering additional states heavy with respect to the Standard Model particles, the scalar and pseudoscalar components of the Higgs doublets and the dark matter candidate. The first example for a UV completion is a Standard Model singlet pseudoscalar a that mixes with the combination $H_1^\dagger H_2$ and serves as the mediator to dark matter,

$$
\begin{aligned}
\mathcal{L} \;=&\; \sum_{i,j=1}^{3} y_{ij}^{u} \bar{Q}_i\, H_1\, u_j \,+\, \sum_{i,j=1}^{3} y_{ij}^{d} \bar{Q}_i\, H_2\, d_j \,+\, \sum_{i,j=1}^{3} y_{ij}^{\ell} \bar{L}_i\, H_2\, \ell_j \\
&+\, \kappa\, a\, H_1^\dagger H_2 \,+\, c_a\, a\, \bar{\chi}\gamma_5\chi \,+\, h.c.\,.
\end{aligned} \tag{3.3}
$$

The implications of this model have been discussed in detail in [44].
The second example arises from more complicated dark sectors, where the dark matter fermion is part of an additional electroweak doublet $\psi = (\chi^+,\, \chi^0)$,

$$
\begin{aligned}
\mathcal{L} \;=&\; \sum_{i,j=1}^{3} y_{ij}^{u} \bar{Q}_i\, H_1\, u_j \,+\, \sum_{i,j=1}^{3} y_{ij}^{d} \bar{Q}_i\, H_2\, d_j \,+\, \sum_{i,j=1}^{3} y_{ij}^{\ell} \bar{L}_i\, H_2\, \ell_j \\
&+\, c_1\, \bar{\psi} H_1 \chi \,+\, c_2\, \bar{\psi} \tilde{H}_2 \chi \,+\, h.c.\,,
\end{aligned} \tag{3.4}
$$

as in doublet-singlet dark matter models. While these UV completions predict very different, model-specific signatures that allow to differentiate between them, the focus of this work is on universal signals that arise in all pseudoscalar mediator models which lead to the EFT in Eq. (3.2).

3.2 Mass generation and Chiral Rotation

The dark matter candidate χ can obtain a mass term via the Higgs mechanism from operators like $H_1^\dagger H_2 \bar{\chi}\chi$, if both Higgs doublets take on their vev. Using this, the effective mass of the dark matter, whose structure is related to the couplings of h to χ[1], is obtained from the Lagrangian in Eq. (3.2) as

$$\mathcal{L}_{m_{eff}} \;=\; 2\,\frac{v_1 v_2}{\Lambda}\left(x_\chi \bar{\chi}\chi + i y_5 \bar{\chi}\gamma^5\chi\right) \;-\; m_\chi \bar{\chi}\chi\,, \tag{3.5}$$

where the shortcuts $c_\chi = x_\chi + i y_\chi$ and $c_5 = x_5 + i y_5$ are used in the case of complex coefficients. From Eq. (3.5) it can easily be seen, that for $y_5 \neq 0$ the total mass is complex. In analogy to [45], we apply a chiral transformation and a field redefinition,

$$\chi \;\to\; \exp(i\gamma^5\theta/2)\chi \quad \text{and} \quad \bar{\chi} \;\to\; \bar{\chi}\exp(i\gamma^5\theta/2)\,, \tag{3.6}$$

with $\exp(i\gamma^5\theta/2) = \cos(\theta/2) + i\gamma^5\sin(\theta/2)$ as $(\gamma^5)^2 = Id$, to deal with the complex mass term. Using this, the operators leading to the mass term in Eq. (3.5) transform as

$$\bar{\chi}\chi \;\to\; \bar{\chi}\exp(i\gamma^5\theta)\bar{\chi} \;=\; \bar{\chi}(\cos\theta + i\gamma^5\sin\theta)\chi\,, \tag{3.7}$$

$$\bar{\chi}\gamma^5\chi \;\to\; \bar{\chi}(\gamma^5\cos\theta - i\sin\theta)\chi\,. \tag{3.8}$$

Inserting this in Eq. (3.5) leads to requirement for a real mass term

$$\tan(\theta) \;=\; \frac{v_1 v_2\, y_5}{m_\chi\Lambda - v_1 v_2 x_\chi}\,. \tag{3.9}$$

With this specific rotation angle and using $v_1 = c_\beta v$ and $v_2 = s_\beta v$, the mass term in Eq. (3.5) and the coefficients in Eq. (3.2) transform as

$$\begin{aligned} m_{eff} \;\to\; m_{\chi,rot} \;&=\; m_\chi c_\theta - \frac{v_1 v_2}{\Lambda}\left(x_\chi c_\theta - y_5 s_\theta\right) \\ &=\; \sqrt{m_\chi^2 - \frac{m_\chi}{\Lambda} x_\chi c_\beta s_\beta v^2 + \frac{v^4}{\Lambda^2} c_\beta^2 s_\beta^2 \left(x_\chi^2 + y_5^2\right)}\,, \end{aligned} \tag{3.10}$$

$$x_\chi \;\to\; x_{\chi,rot} = x_\chi c_\theta - y_5 s_\theta \;=\; \frac{m_\chi x_\chi - c_\beta s_\beta \frac{v^2}{\Lambda}\left(x_\chi^2 + y_5^2\right)}{m_{\chi,rot}}\,, \tag{3.11}$$

$$y_\chi \;\to\; y_{\chi,rot} = x_5 s_\theta + y_\chi c_\theta\,, \tag{3.12}$$

$$x_5 \;\to\; x_{5,rot} = x_5 c_\theta - y_\chi s_\theta\,, \tag{3.13}$$

$$y_5 \;\to\; y_{5,rot} = x_\chi s_\theta + y_5 c_\theta \;=\; \frac{m_\chi}{m_{\chi,rot}}\, y_5\,. \tag{3.14}$$

The additional t_β-dependence makes the analyses more complicated. But it is possible to choose c_χ and c_5 such that the values used in the later analyses are recovered and approximately constant for $t_\beta < 3$.

[1] As v_1 and v_2 have no α dependent prefactors all results are independent of $c_{\beta-\alpha}$.

A model in which χ gets all mass from this Higgs mechanism is excluded by a combination of relic density and direct detection constraints as discussed in more detail in the next section. There it is shown that Re$[C_\chi] = x_\chi v/\Lambda$ has to be small. In addition Im$[C_5]$ has to be zero to conserve CP symmetry, which we assume throughout this work. Because of that we introduced the explicit mass term proportional to m_χ softly breaking the symmetry.
Therefore, for the rest of the work we choose Re$[C_\chi] \ll 1$ and Im$[C_5] = 0$ and the dark matter mass generated by the Higgs mechanism is small or even zero.

3.3 Higgs Couplings and Decay Widths

After electroweak symmetry breaking, and choosing the mass eigenstate basis, the dark matter couplings in Lagrangian in Eq. (3.2) can be written as

$$\begin{aligned}\mathcal{L}_{Yuk} &= g_{h\chi}\, h\, \bar{\chi}\chi + g_{h5}\, h\, \bar{\chi}\gamma_5\chi + g_{H\chi}\, H\, \bar{\chi}\chi + g_{H5}\, H\, \bar{\chi}\gamma_5\chi + \\ &\quad g_{A\chi}\, A\, \bar{\chi}\chi + g_{A5}\, A\, \bar{\chi}\gamma_5\chi\,,\end{aligned} \tag{3.15}$$

where the couplings of the neutral scalars to χ are given by

$$g_{h\chi} = \left(\frac{2\,(c_{\beta-\alpha} + t_\beta s_{\beta-\alpha})}{1+t_\beta^2} - c_{\beta-\alpha}\right) \mathrm{Re}[C_\chi]\,, \tag{3.16}$$

$$g_{h5} = \left(\frac{2\,(c_{\beta-\alpha} + t_\beta s_{\beta-\alpha})}{1+t_\beta^2} - c_{\beta-\alpha}\right) \mathrm{Im}[C_5]\,, \tag{3.17}$$

$$g_{H\chi} = \left(\frac{2\,(c_{\beta-\alpha} t_\beta - s_{\beta-\alpha})}{1+t_\beta^2} + s_{\beta-\alpha}\right) \mathrm{Re}[C_\chi]\,, \tag{3.18}$$

$$g_{H5} = \left(\frac{2\,(c_{\beta-\alpha} t_\beta - s_{\beta-\alpha})}{1+t_\beta^2} + s_{\beta-\alpha}\right) \mathrm{Im}[C_5]\,, \tag{3.19}$$

$$g_{A\chi} = \mathrm{Im}[C_\chi]\,, \tag{3.20}$$

$$g_{A5} = \mathrm{Re}[C_5]\,. \tag{3.21}$$

and we define $C_\chi = c_\chi v/\Lambda$ and $C_5 = c_5 v/\Lambda$. The charged Higgs does not couple to dark matter at tree-level. The couplings proportional to the imaginary parts of c_χ (c_5) induce CP violating couplings of the scalars (pseudoscalar) to the dark sector. This do not have to be a problem since the properties of the dark sector are unknown, but for simplicity we take c_χ and c_5 to be real for the rest of this work[2].

[2] CP violating couplings might lead to interesting phenomenology if it could be connected to CP violation in the visible sector, which is needed to explain the baryon-asymmetry.

In the alignment limit $c_{\beta-\alpha} = 0$ these couplings simplify to

$$g_{h\chi} = \frac{2\,t_\beta}{1+t_\beta^2}\,\mathrm{Re}[C_\chi]\,, \tag{3.22}$$

$$g_{h5} = \frac{2\,t_\beta}{1+t_\beta^2}\,\mathrm{Im}[C_5]\,, \tag{3.23}$$

$$g_{H\chi} = \left(1-\frac{2}{1+t_\beta^2}\right)\mathrm{Re}[C_\chi] = c_{2\beta}\,\mathrm{Re}[C_\chi]\,, \tag{3.24}$$

$$g_{H5} = \left(1-\frac{2}{1+t_\beta^2}\right)\mathrm{Im}[C_5] = c_{2\beta}\,\mathrm{Im}[C_5]\,, \tag{3.25}$$

$$g_{A\chi} = \mathrm{Im}[C_\chi]\,, \tag{3.26}$$

$$g_{A5} = \mathrm{Re}[C_5]\,. \tag{3.27}$$

After introducing the dark matter couplings, we are able to calculate all relevant partial decay widths for the heavy scalar H, the charged scalar $H^\pm$ and the pseudoscalar A in the alignment limit $c_{\beta-\alpha} = 0$. Here we just take the CP conserving couplings into account. For the light scalar h, which is associated with the Standard Model Higgs in this limit, only the partial decay width to dark matter is shown because the other widths do not change compared to the Standard Model. Of course the branching ratios change as the total width increases.
Offshell decays and those that only become relevant for $c_{\beta-\alpha} > 0$ are not shown.In all plots branching ratios smaller than 1% are not shown.
For the heavy scalar H, the dominating partial decay widths are

$$\Gamma(H\to t\bar{t}) = \frac{3}{8\pi}\frac{m_t^2}{v^2}\,\kappa_{Hu}^2\,M_H\left(1-\frac{4m_t^2}{M_H^2}\right)^{3/2}, \tag{3.28}$$

$$\Gamma(H\to \chi\bar{\chi}) = \frac{1}{8\pi}\,g_{H\chi}^2\,M_H\left(1-\frac{4m_\chi^2}{M_H^2}\right)^{3/2}, \tag{3.29}$$

$$\Gamma(H\to ZA) = \frac{g_W^2}{64\pi}\frac{\left(M_A^4+(M_H^2-M_Z^2)^2-2M_A^2(M_H^2+M_Z^2)^2\right)^{3/2}}{M_H^3M_W^2}, \tag{3.30}$$

$$\Gamma(H\to AA) = \frac{1}{32\pi}\frac{(M_A^2-M_H^2)^2}{v^2M_H}\frac{(t_\beta^2-1)^2}{t_\beta}\left(1-\frac{4M_A^2}{M_H^2}\right)^{1/2}, \tag{3.31}$$

where the couplings κ_{Hu} and $g_{H\chi}$ are defined in Table 2.2 and Eq. (3.24).
The branching ratios for $M_H = M_{H^\pm} = 500$ GeV , $c_5 = 0$, $c_\chi = 1$, and $m_\chi = 1$ GeV are shown in Figure 3.1. The left panel shows the dependence in M_A for $t_\beta = 1$ and the right panel shows the t_β-dependence for $M_A = 200$ GeV. Because the dominant branching fractions of H do not depend on the Yukawa sector of the 2HDMs under consideration, both panels of Figure 3.1 hold for 2HDMs of type I and type II. For

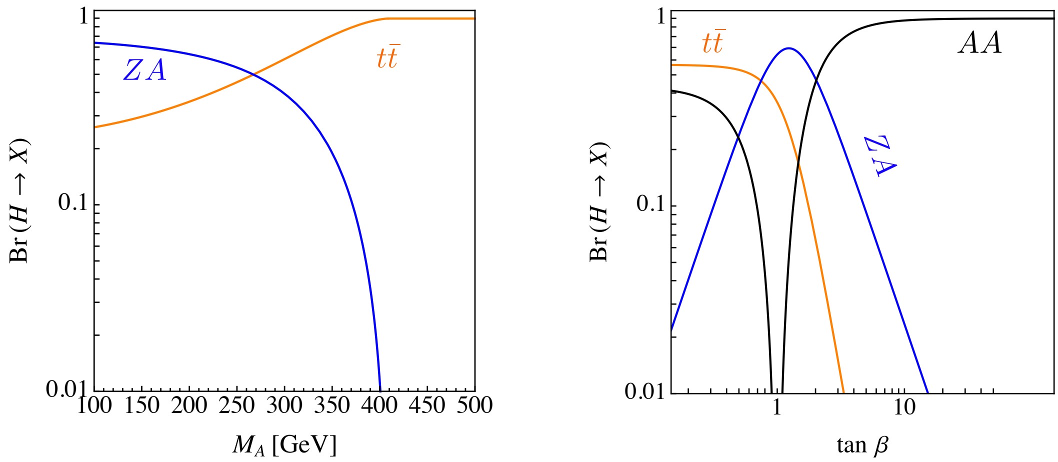

Figure 3.1: The dominant branching ratios ($> 1\%$) of the heavy scalar H are shown for $M_H = M_{H^\pm} = 500$ GeV, $c_{\beta-\alpha} = 0$, $C_5 = 0$, $C_\chi = 1$, and $m_\chi = 1$ GeV.
Left: In dependence of the pseudoscalar mass M_A and $t_\beta = 1$.
Right: In dependence of t_β for fixed pseudoscalar mass $M_A = 200$ GeV, the relevant branching ratios are independent of the type of a 2HDM.

masses $M_H > M_A + M_Z$ and $2 \gtrsim t_\beta \gtrsim 0.7$, the dominant branching fraction is $H \to ZA$, giving rise to a mono-Z final state for the dominant decay channel of $A \to \chi\bar{\chi}$. For larger values of t_β the decay to AA dominates, as shown in Eq. (3.31) this branching ratio is zero for $t_\beta = 1$. For larger pseudoscalar masses and $t_\beta = 1$, the di-top final state is dominant and more promising for direct searches. It is intriguing that the parameter space giving rise to a mono-Z signal agrees with the bounds discussed in the following chapter.
For the pseudoscalar A, the following partial decay widths are relevant

$$\Gamma(A \to t\bar{t}) = \frac{3}{8\pi}\frac{m_t^2}{v^2}\,\kappa_{Au}^2\,M_A\left(1 - \frac{4m_t^2}{M_A^2}\right)^{1/2}, \tag{3.32}$$

$$\Gamma(A \to b\bar{b}) = \frac{3}{8\pi}\frac{m_b^2}{v^2}\,\kappa_{Ad}^2\,M_A\left(1 - \frac{4m_b^2}{M_A^2}\right)^{1/2}, \tag{3.33}$$

$$\Gamma(A \to \tau^+\tau^-) = \frac{1}{8\pi}\frac{m_\tau^2}{v^2}\,\kappa_{A\ell}^2\,M_A\left(1 - \frac{4m_\tau^2}{M_A^2}\right)^{1/2}, \tag{3.34}$$

$$\Gamma(A \to \chi\bar{\chi}) = \frac{1}{8\pi}\,g_{A5}^2\,M_A\left(1 - \frac{4m_\chi^2}{M_A^2}\right)^{1/2}, \tag{3.35}$$

and $\Gamma(A \to c\bar{c})$ follows from $\Gamma(A \to t\bar{t})$ with the replacement $m_t \to m_c$. The main branching ratios in dependence of M_A are plotted in the left panel of Figure 3.2 for $t_\beta = 1$, $M_H = M_H^\pm = 500$ GeV, $C_5 = 1$, $C_\chi = 0$, and $m_\chi = 1$ GeV. As long as C_5 is roughly of order one the decay to χ clearly dominates between $M_A > 2m_\chi$ and

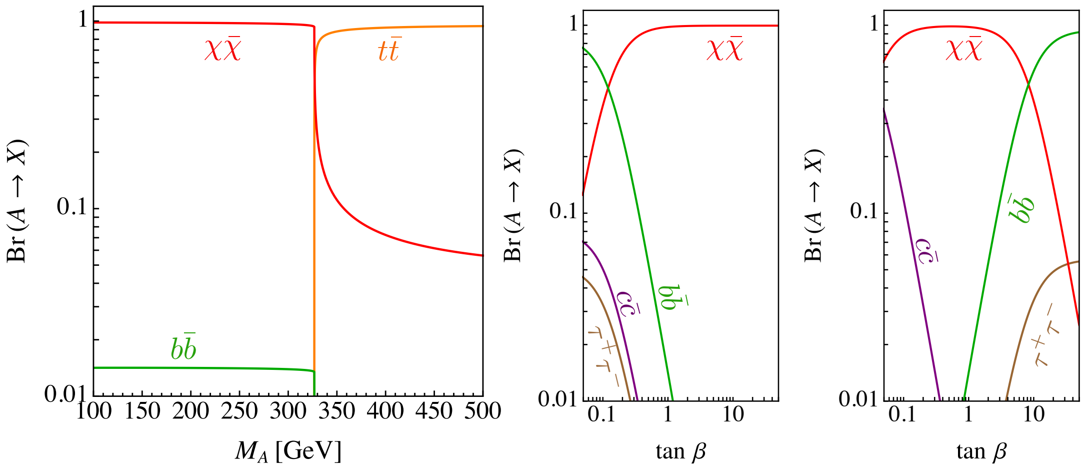

Figure 3.2: The dominant branching ratios ($> 1\%$) of the pseudoscalar A are shown for $M_H = M_{H^\pm} = 500$ GeV, $c_{\beta-\alpha} = 0$, $C_5 = 1$, $C_\chi = 0$, and $m_\chi = 1$ GeV.
Left: In dependence of the pseudoscalar mass M_A and $t_\beta = 1$.
Center (right): In dependence of t_β for fixed pseudoscalar mass $M_A = 200$ GeV with Yukawa couplings as in a 2HDM of type I (II).

the top threshold at $M_A = 2m_t$. For lower pseudoscalar masses BR$(A \to b\bar{b})$ and for higher masses BR$(A \to t\bar{t})$ dominates. Changing C_5 does not change the findings qualitatively and increasing m_χ only shifts the region described above.
The center (right) panel of Figure 3.2 shows the dominant branching ratios in dependence of t_β in 2HDMs of type I (II) for $M_A = 200$ GeV, and again $C_5 = 1$, $C_\chi = 0$, $m_\chi = 1$ GeV and $M_H = M_{H^\pm} = 500$ GeV. In type I the coupling to $b\bar{b}$ is proportional to $1/t_\beta$ and therefore dominates for $t_\beta \ll 1$. In type II the decay to $c\bar{c}$ dominates for small t_β, as long as $M_A < 2m_t$, and for higher values of t_β decays to $b\bar{b}$ and $\tau^+\tau^-$ are getting important. For $t_\beta = \mathcal{O}(1)$, the most important region for us, the decay to dark matter clearly dominates.
For the heavy charged scalar $H^\pm$ we find

$$\Gamma(H^+ \to t\bar{b}) = \frac{3}{8\pi} \frac{|V_{tb}|^2}{M_{H^\pm} v^2} \lambda(m_t^2, m_b^2, M_{H^\pm}^2)^{1/2} \Big(\big(M_{H^\pm}^2 - m_t^2 - m_b^2\big) \big(m_b^2 \kappa_{Ad}^2 + m_t^2 \kappa_{Au}^2\big) - 4 m_t^2 m_b^2 \Big) , \tag{3.36}$$

$$\Gamma(H^+ \to \tau^+ \nu) = \frac{1}{8\pi} \frac{1}{M_{H^\pm} v^2} m_\tau^2 \kappa_{A\ell}^2 \left(1 - \frac{m_\tau^2}{M_{H^\pm}^2}\right)^3 , \tag{3.37}$$

$$\Gamma(H^+ \to A W^+) = \frac{1}{16\pi c_W^2} \frac{M_W^4}{M_{H^\pm} v^2} \lambda(M_A^2, M_W^2, M_{H^\pm}^2)^{1/2} \lambda(M_A^2, M_{H^\pm}^2, M_W^2) , \tag{3.38}$$

where $\lambda(x, y, z) = ((x + y - z)^2 - 4xy)/z^2$. The dependence of the branching ratios on M_A is shown on the left panel of Figure 3.3 for $M_H = M_{H^\pm} = 500$ GeV, $t_\beta = 1$,

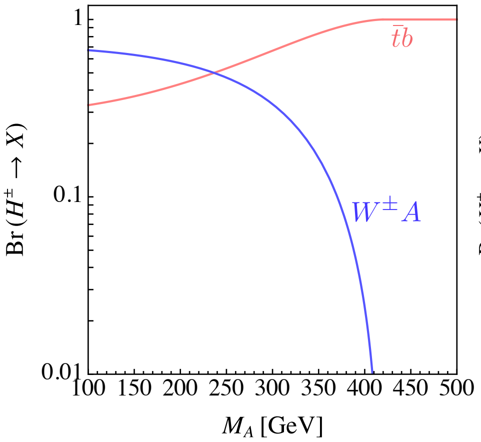

Figure 3.3: The dominant branching ratios ($> 1\%$) of the charged scalar $H^\pm$ are shown for $M_H = M_{H^\pm} = 500$ GeV, $c_{\beta-\alpha} = 0$, and arbitrary dark matter couplings as they do not matter.
Left: In dependence of the pseudoscalar mass M_A and $t_\beta = 1$.
Center (right): In dependence of t_β for fixed pseudoscalar mass $M_A = 200$ GeV with Yukawa couplings as in a 2HDM of type I (II).

and arbitrary dark matter couplings as they do not matter. On the center (right) panel of Figure 3.3 the t_β-dependence of the branching ratios of the charged scalar are shown for fixed $M_A = 200$ GeV and the Yukawa couplings as in a 2HDM of Type I (II). For $t_\beta \gtrsim 1$ the BR$(H^\pm \to W^\pm A)$ dominates as long as the decay is kinematically allowed. This could give rise to a mono-$W^\pm$ signal as A mainly decays into dark matter.
In the alignment limit the decay widths of h are unchanged, because $\kappa_{hf} = 1$ for all Standard Model fermions f and the couplings to gauge bosons are also unchanged. There is just an additional decay channel to dark matter with

$$\Gamma(h \to \chi\bar{\chi}) = \frac{1}{8\pi} g_{h\chi}^2 m_h \left(1 - \frac{4m_\chi^2}{m_h^2}\right)^{3/2} . \tag{3.39}$$

This channel dominates as long as χ is heavier than $3m_b$ and lighter than $m_h/2$.

3.4 Further Operators

In this section we shortly describe possible modifications of the Lagrangian in Eq. (3.2), either by adding further operators breaking the assumed symmetries or by assigning a different charge to $\chi\bar{\chi}$.

Breaking of the Symmetry

Assuming neither CP conservation nor the additional global symmetry in the dark sectors, operators proportional to $H_i^\dagger H_i$, $i = 1, 2$, can be added to Eq. (3.2)

$$\Delta\mathcal{L} = \left(c_{\chi,1} \frac{H_1^\dagger H_1}{\Lambda} + c_{\chi,2} \frac{H_2^\dagger H_2}{\Lambda} \right) \bar{\chi}\chi + \left(c_{5,1} \frac{H_1^\dagger H_1}{\Lambda} + c_{5,2} \frac{H_2^\dagger H_2}{\Lambda} \right) \bar{\chi}\gamma_5\chi + h.c. , \tag{3.40}$$

where the coefficients $c_{\chi,i}$ and $c_{5,2}$, $i = 1, 2$, are real because of unitarity.
They give rise to new scalar couplings of χ to the scalars h and H, but not to new couplings to the pseudoscalar A as those terms cancel against their hermitian conjugates. The resulting couplings have a different t_β-dependence than $g_{h\chi}$ in Eq. (3.18). In the alignment limit $c_{\chi,1}$ goes with an additional factor $1/t_\beta$ and $c_{\chi,2}$ with t_β.

Higher Order Insertions

There is no need for the $H_1^\dagger H_2$ to carry the same charge as $\chi\bar{\chi}$. In general the case the effective Lagrangian reads as

$$\mathcal{L} = c_\chi \frac{\left(H_1^\dagger H_2\right)^n}{\Lambda^{2n-1}} \bar{\chi}\chi + c_5 \frac{\left(H_1^\dagger H_2\right)^n}{\Lambda^{2n-1}} \bar{\chi}\gamma^5\chi - m_\chi\bar{\chi}\chi + h.c. , \tag{3.41}$$

where $\chi\bar{\chi}$ carries a charge of n relative to $H_1^\dagger H_2$. In the later analyses the case $n = 2$ is briefly discussed, but higher cases are also possible in principle. All scenarios with $n > 1$ have much more complicated couplings and multi-particle vertices of the scalars and the pseudoscalar to dark matter than the $n = 1$ case, which are beyond the scope of this work.

4 Experimental Constraints from different Sources

In this chapter we discuss different experimental and theoretical constraints relevant for the model presented in the previous chapter. For the scalar sector we consider bounds from Higgs and flavor physics, electroweak precision observables, collider searches for heavy resonances and stability requirements. The dark sector is constrained by results from the relic density, direct and indirect detection experiments and mono-X searches at the LHC.
We are able to find reasonable intervals for the open parameters, where all experimental constraints are taken into account and predictions are possible.

4.1 Higgs Couplings

Adding a second Higgs doublet and the new decay channel to χ changes the couplings, the branching ratios as well as the total width of the light scalar h identified with the Standard Model Higgs. Therefore, measuring the Higgs coupling strength in several channels puts strong constraints on any possible mixing of the Higgs with new scalar degrees of freedom[1] and couplings to new invisible states.
Since it is not possible to measure the production cross section or the branching ratio for a specific channel directly, the experimentally measured value for a production channel i and a decay channel f is expressed by the signal strength

$$\mu_i^f \;=\; \frac{\sigma_i}{\sigma_i^{\mathrm{SM}}}\,\frac{B^f}{(B^f)^{\mathrm{SM}}} \;=\; \frac{\sigma_{\mathrm{i}}}{\sigma_{\mathrm{i}}^{\mathrm{SM}}}\,\frac{\Gamma(h\to f)}{\Gamma(h\to f)^{\mathrm{SM}}}\,\frac{\Gamma_h^{\mathrm{SM}}}{\Gamma_h}\,, \tag{4.1}$$

where σ_i denotes the production cross section, B^f the branching ratio of h to the final state f and Γ_h the total width of h [47]. The superscript SM denotes the Standard Model predictions. We consider $i = V, t$ and $f = ZZ$, WW, $\gamma\gamma$, bb, $\tau\tau$, $\mu\mu$, where V stands for the combination of vector boson fusion (VBF) and vector boson associated (VH) production and t for gluon fusion and $t\bar{t}$ production because the amplitude modulations are the same in our model, so we put them together to get better results.

[1] For simplified models in which the Higgs mixes with a scalar mediator that couples to dark matter, measurements of Higgs couplings provide a stronger bound on the mixing angle than any mono-X search [46].

The deviations of the Higgs couplings in a 2HDM from the Standard Model couplings are parametrized by the coupling modifiers κ_{hj}, given in Table 2.2, fulfilling the relations

$$\kappa_{hj} = \frac{g_{jjh}}{g_{jjh}^{\text{SM}}} \quad \text{or} \quad \kappa_{hj}^2 = \frac{\sigma_j}{\sigma_j^{\text{SM}}} \quad \text{or} \quad \kappa_{hj}^2 = \frac{\Gamma(h \to j)}{\Gamma(h \to j)^{\text{SM}}}\,, \tag{4.2}$$

In addition, the modifications of the couplings to the vector bosons $V = W^{\pm}$, Z are given by

$$\kappa_{hV} = s_{\beta-\alpha}\,. \tag{4.3}$$

If m_χ is smaller than $m_h/2$, χ offers an additional decay channel for h with partial width $\Gamma(h \to \chi\bar{\chi})$ given in Eq. (3.39). In this case the total width is given by

$$\Gamma_{\text{tot}} = \Gamma(h \to \chi\bar{\chi}) + \kappa_{\text{tot}}^2\,\Gamma_h^{\text{SM}}\,, \tag{4.4}$$

where we defined

$$\kappa_{tot}^2 = \sum_j \left(B^j\right)^{\text{SM}} \kappa_{hj}^2 = \sum_j \frac{\Gamma(h \to j)}{\Gamma_h^{\text{SM}}}\,. \tag{4.5}$$

With these definitions the signal strength can be written as

$$\mu_i^f = \Gamma_h^{\text{SM}}\,\frac{\kappa_i^2\,\kappa_{\text{tot}}^2}{\Gamma(h \to \chi\bar{\chi}) + \kappa_{\text{tot}}^2\Gamma_h^{\text{SM}}} = \kappa_{hi}^2\,\kappa_{\text{tot}}^2\,\frac{\Gamma_h^{\text{SM}}}{\Gamma^{\text{tot}}}\,. \tag{4.6}$$

In Figure 4.1, we present a global fit to the Higgs signal strength measurements based on the combination of CMS and ATLAS signal strength measurements presented in [47] at $\sqrt{s} = 7$ TeV with 5 fb^{-1} amount of data and 20 fb^{-1} at 8 TeV. An additional constraint arises from the bound on invisible Higgs decays Br$(h \to$ invisible$) < 0.23$ [48, 49].

We consider the generic scenario of 2HDMs of type I (left panel) and type II (right panel) for which no couplings to dark matter are present, that is $C_\chi = 0$. The allowed parameter space for this case is shaded gray. We further show the global fit for three additional values of $C_\chi = 2 \times 10^{-4}, 10^{-3}, 6 \times 10^{-3}$ where we fix $\Lambda = 1$ TeV with the respective parameter space allowed by all constraints shaded yellow, orange and red. The dark matter mass has been fixed to $m_\chi = 0$. The parameter Im$[C_5]$ also allows for Higgs couplings to dark matter, but leads to the same results, up to a weaker sensitivity on the dark matter mass in the case of the pseudoscalar coupling. The parameter space that survives for large values of Re$[C_\chi]$ or Im$[C_5]$ corresponds to the region in which $g_{h\chi} = g_{h5} = 0$. This parameter space is not stable under additional contributions from loop-induced Higgs couplings or additional operators, such as $H_i H_i^\dagger \bar{\chi}\chi$, $i = 1, 2$. There is also a small band of allowed values for type II, where $\kappa_{hd} = -1$ and up to now no

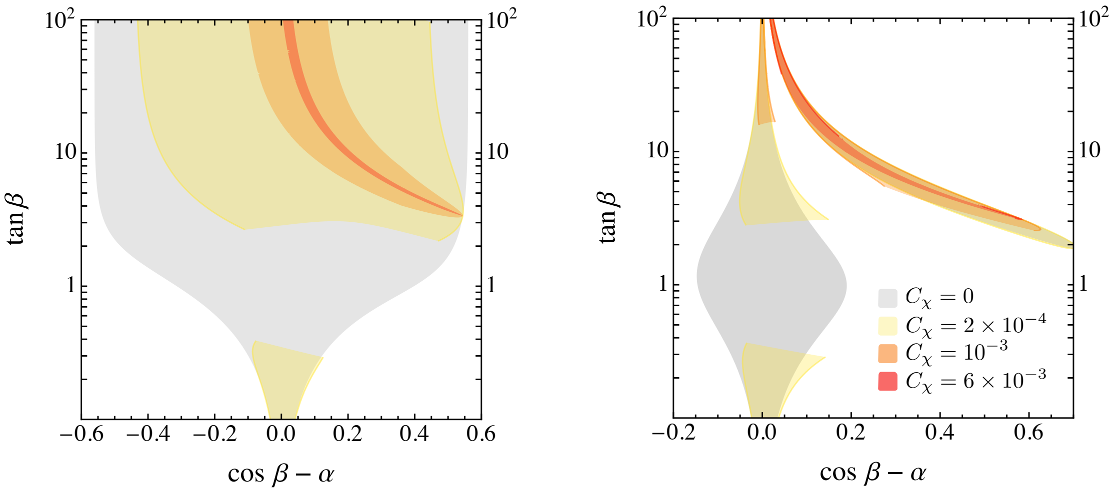

Figure 4.1: Allowed parameter space for 2HDM of Type I (left) and II (right) after fitting the couplings to the Higgs signal strength measurement from [47]. Colored regions are allowed for an increasing dark matter coupling. This yields us to the alignment limit, $c_{\beta-\alpha} = 0$, and $m_\chi > M_h/2$. Figure from [46].

measurement can distinguish between plus and minus one. And coincidentally $g_{h\chi}$ in Eq. (3.16) is roughly zero for the same values of $c_{\beta-\alpha}$ and t_β, therefore, it is allowed even for higher values of C_χ. But this region is unstable, in the sense that one has to fix the parameters very precisely. Because of that, we concentrate on the alignment limit $c_{\beta-\alpha} \simeq 0$.
It follows therefore, that either the Wilson coefficients Re$[C_\chi]$ and Im$[C_5]$ are severely suppressed, or the Higgs decay to dark matter needs to be kinematically disallowed. Other scenarios are excluded by Higgs coupling strength measurements even in the alignment limit.

4.2 Flavor Physics

Natural flavor conservation ensures the absence of tree-level flavor changing neutral currents (FCNCs) mediated by h, H and A. The new charged scalar allows for new flavor changing currents at one-loop level. The most stringent bounds for this kind of models come from measurements of the decay $b \to s\gamma$ based on the Belle dataset. This requires $M_{H^\pm} > 569 - 795$ GeV for 2HDMs of type II and $M_{H^\pm} > 268 - 504$ GeV for 2HDMs of type I and $t_\beta = 1$ at 95% C.L., where the range depends on the method applied to derive that bound [50].
While this constraint is rather independent from t_β for 2HDMs of type II, it scales like $1/t_\beta^2$ in the case of 2HDMs of type I. As a consequence, for $t_\beta > 2$, flavor constraints become less important than collider searches for the latter case. Anticipating the unitarity and perturbativity bounds derived below, large values of t_β are strongly disfavored

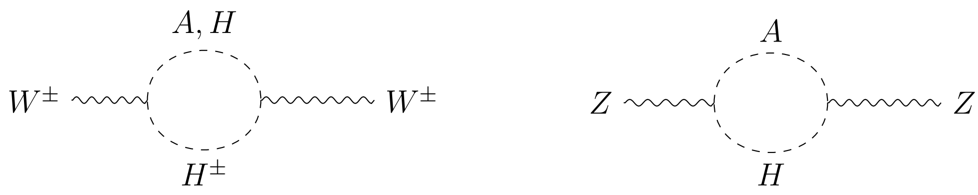

Figure 4.2: Feynman diagrams of example loop contributions of different combinations of the scalars of the 2HDM adding to the Standard Model $W^{\pm}$ and Z mass. Drawn with [51].

even for 2HDMs of type I and we adopt the constraint $M_{H^{\pm}} > 500$ GeV in the following.
It should be stressed that indirect bounds are subject to change if more complete models are considered and contributions from additional particles, like a new heavy charged fermion running in the loop, to the relevant observables are taken into account.

4.3 Electroweak Precision Observables

The charged and heavy scalars and the pseudoscalar give rise to different contributions at one-loop level to the $W^{\pm}$ and Z bosons mass, such that the tree-level relation between the Z and $W^{\pm}$ boson masses set by electroweak symmetry breaking is broken [52].. While for the Z a pair of charged scalars or the pseudoscalar plus an uncharged scalar is in the loop, for the $W^{\pm}$ it is always a $H^{\pm}$ plus a neutral (pseudo-) scalar, example diagrams are shown in Figure 4.2.
The ρ-parameter is proportional to the ratio of the two masses and measured very close to 1, within the Standard Model prediction. Therefore at least two of the masses has to be equal, as shown in Figure 4.3. In the left panel the allowed mass combinations are marked in orange and $M_{H^{\pm}} = 500$ GeV. The right panel, where $M_H = 500$ GeV, shows that we are forced to be close to the alignment limit $c_{\beta-\alpha} \to 0$ as we want to have M_A as a free parameter.
These effects are independent of t_β, because the couplings of the scalars and the pseudoscalar to gauge bosons only depend on $c_{\beta-\alpha}$. The corresponding constraints are therefore valid for 2HDMs of type I and type II and constrain the mass splittings between the heavy spin 0 mass eigenstates M_H, M_A and M_{H^+} and the mixing angle $c_{\beta-\alpha}$. Taking into account the preference for the alignment limit of the global fit to Higgs signal strength measurements, and flavor constraints, we show the allowed parameter space by a 95% C.L. fit to the oblique parameters S, T and U in the $M_A - M_H$ plane for fixed $M_{H^{\pm}} = 500$ GeV and $c_{\beta-\alpha} = 0$ on the left panel of Figure 4.3. A clear preference for almost degenerated masses $M_H \approx M_{H^{\pm}}$ or $M_H \approx M_A$ is evident. This can be understood by the restoration of the global custodial symmetry present in the Standard Model Higgs potential in the full 2HDM scalar potential in these limits. Since we are interested

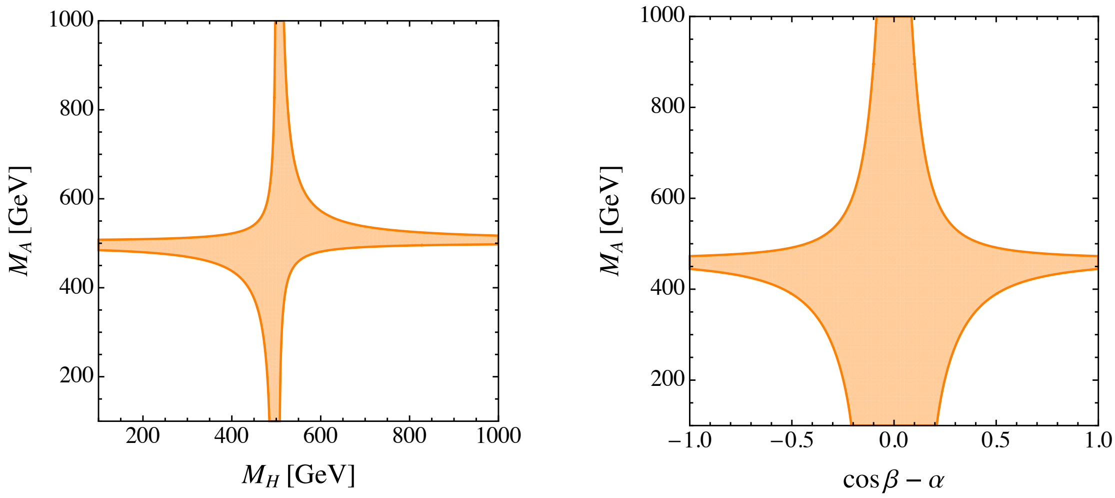

Figure 4.3: Left: Parameter space allowed by a combined fit to the oblique parameters at the 95% C.L. in the $M_H - M_A$ plane for $M_{H^+} = 500$ GeV and $c_{\beta-\alpha} = 0$. Right: Parameter space allowed by a combined fit to the oblique parameters at the 95% C.L. in the $c_{\beta-\alpha} - M_A$ plane for fixed masses of $M_H = M_{H^+} = 500$ GeV. Figure from [46].

in scanning the range of pseudoscalar mediators, we choose $M_H = M_{H^\pm} = 500$ GeV and present the allowed parameter space in the $c_{\beta-\alpha} - M_A$ plane. Apart from a fully degenerate spectrum $M_A \approx M_H \approx M_{H^\pm}$, electroweak precision constraints prefer the alignment limit and in the case of 2HDMs of type I result in a stronger constraint on $c_{\beta-\alpha}$ than the global fit to Higgs coupling strength measurements for $t_\beta \gtrsim 1$. As in the case of flavor observables, it should be stressed that the constraints from electroweak precision observables are indirect and sensitive to the presence of additional particles charged under $SU(2)_L \times U(1)_Y$, which can lead to cancellations in complete models. The bounds presented here should therefore only serve as a guideline.

4.4 Stability, Perturbativity and Unitarity

We consider the stability and perturbativity bounds on the scalar potential coefficients given in Eq. (2.11) and (2.12). In addition, the requirement of unitarity of the scattering amplitudes between scalars introduces strong bounds on the potential coefficients. Partial wave unitarity translates into the condition that the eigenvalues of the relevant submatrices of the scattering matrix have eigenvalues s_i with $|s_i| < 8\pi$ for all i [53, 46].
As the coefficients are connected to t_β and $c_{\beta-\alpha}$ via the relations in Eq. (2.13) to (2.19) and the masses are already fixed to $M_H = M_{H^\pm} = 500$ GeV, those requirements lead to strong constraints on t_β and $c_{\beta-\alpha}$. In particular, a large mass splitting $M_A < M_H, M_{H^\pm}$

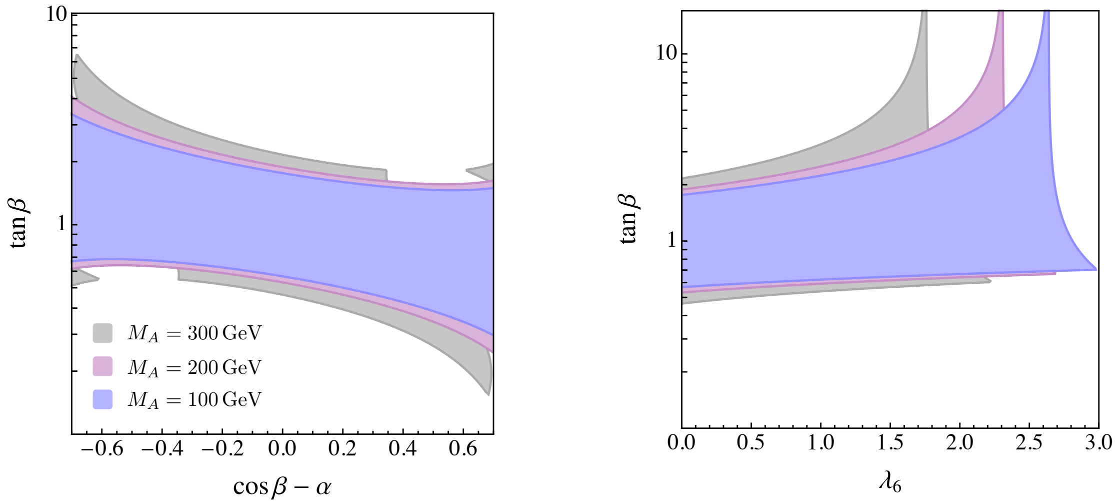

Figure 4.4: Left: Parameter space allowed by stability, unitarity and perturbativity constraints in the $c_{\beta-\alpha} - t_\beta$ plane for $M_H = M_{H^\pm} = 500$ GeV and three different values of pseudoscalar masses $M_A = 100$ GeV (blue), 200 GeV (purple) and 300 GeV (gray). Right: The effect of a non-vanishing quartic coupling λ_6 on the parameter space in the alignment limit $c_{\beta-\alpha} = 0$. Figure from [46].

requires sizable quartic couplings and is therefore constrained by perturbativity and unitarity.

In the left panel of Figure 4.4, we show the parameter space allowed by stability, unitarity and perturbativity constraints in the $c_{\beta-\alpha} - t_\beta$ plane for $M_H = M_{H^\pm} = 500$ GeV and three values for the pseudoscalar mass $M_A = 100$ GeV (blue), 200 GeV (purple) and 300 GeV (gray). Taking into account the constraint from electroweak precision observables, which force $|c_{\beta-\alpha}| \lesssim 0.2$ for these masses, it results in the constraint $0.4 \lesssim t_\beta \lesssim 3$.

We note, that this constraint can be considerably relaxed in more general models which allow for additional quartic couplings. As an example, we show the effect of adding the quartic coupling $\Delta V_H = \lambda_6 H_1^\dagger H_1\, H_1 H_2^\dagger + h.c.$ to the potential in Eq. (2.10) and varying it for real values $\lambda_6 = 0 - 3$ in the right panel of Figure 4.4. In this scenario, larger values of t_β are possible for specific values of λ_6, but are still disfavored with respect to smaller values of $t_\beta = \mathcal{O}(1)$.

Additional perturbativity constraints can be derived for the Yukawa couplings in Eq. (3.15). In particular the top Yukawa coupling becomes non-perturbative for $t_\beta \lesssim 0.3$ for 2HDMs of type I and type II. This constraint is automatically fulfilled once the stability, perturbativity and unitarity constraints on the scalar potential are taken into account.

4.5 Collider Searches

Collider searches for the heavy resonances A, $H^{\pm}$ and H directly constrain their masses and couplings to Standard Model particles. We consider only the alignment limit $c_{\beta-\alpha} = 0$, preferred by Higgs and electroweak precision bounds. In this case, for the pseudoscalar A, only couplings to fermions are relevant. The branching ratios, shown in Figure 3.2, are dominated by the decay to dark matter, therefore the exclusion limits are very weak. Direct searches for the new heavy resonances can only exclude values of $t_\beta \lesssim 0.3$, which is significantly below the exclusion limits of mono-X searches presented in the following section [46].
The masses of $H^{\pm}$ and H are pushed to high values by flavor and electroweak precision observables such that in our setup collider searches are not able to put stronger bounds on them [46].

4.6 Direct Detection

After constraining the scalar part, we use results from direct and indirect detection experiments and the requirement of getting the correct relic density to constrain the parameters of the dark sector. All numerical calculations in this and the following two sections are carried out with MicrOmegas version 4.3.1 [20, 21] based on a CH output written with FeynRules version 2.3.24 [54, 55]. The corresponding FeynRules[2] file will be uploaded to the FeynRules database soon. The coefficients of the Yukawa part are checked and agree with [42]. Likewise, the trilinear and quartic Higgs self-couplings are in full agreement with the results in [56, 57, 52].
Modern direct detection experiments, like XENON1T or LUX, give the strongest constraints to the WIMP-nucleus cross sections. For example, they exclude scalar portals for a wide range of parameter space. But scattering amplitudes from interaction structures proportional to $\bar{f}\gamma^5 f$ are velocity suppressed and, therefore, vanish for cold dark matter [34, 33]. If this structure appears at least in one vertex of the scattering diagram, the corresponding couplings are effectively not constrained by direct detection experiments. In our model only Re(C_χ), or Re(C_χ^{new}) after chiral rotation, are constrained, as they lead to scalar couplings of the Standard Model fermions to $\chi\bar{\chi}$ via h and H.
For an upper bound on Re(C_χ) the spin-independent χ-nucleus cross section is compared to the newest exclusion limit at 90% confidence level from the XENON1T experiment [30]. The spin-dependent cross section is found to be zero in our model. For simplicity we only considered the best value of $\sigma^{\text{XENON1T}}_{\chi-nucleon} \approx 10^{-47}$ cm^2 for $m_\chi \approx 30$ GeV and neglect the mass dependence of the measurement, cf. Figure 1.5. Therefore for higher dark matter masses we slightly overestimate the exclusion limits. In the alignment limit $g_{h\chi}$ has its maximum at $t_\beta = 1$ while the couplings to Standard Model

[2]It is based on the FeynRules model file "The general Two-Higgs Doublet Model" from http://feynrules.phys.ucl.ac.be/view/Main/2HDM.

fermions are constant. Therefore, the strongest bound for Re(C_χ) is obtained for $t_\beta = 1$ and $m_\chi = 30$ GeV. In this case, we found Re$(C_\chi) \lesssim 1.1 \times 10^{-2}$. For other m_χ or t_β, slightly higher values of Re(C_χ) are allowed, but not considered here. It should be mentioned that for $m_\chi < m_h/2$ measurements of the Higgs couplings, presented in Section 4.1, lead to stronger constraints on Re(C_χ). For the pseudoscalar mediator, with couplings proportional to Re(C_5) the dark matter-nucleus cross section is zero, as expected.

4.7 Relic Density

As mentioned before, direct detection experiments are not able to constrain pseudoscalar mediators with couplings proportional to $C_5 \bar{f}\gamma_5 f$. The requirement of getting the correct relic abundance $\Omega_\chi h^2$ is a better way to constrain the dark matter parameters m_χ and C_5.
In order to estimate the order of magnitude of C_5 for reasonable values of the relic density, we scan over C_5 and m_χ for $t_\beta = 1$ and several pseudoscalar masses M_A between 80 and 350 GeV. In Figure 4.6 we show plots for $M_A = 160$ and $M_A = 250$ GeV. In a second step a scan over m_χ and t_β with fixed values for C_χ, C_5 and various values for M_A is performed. Again plots for $M_A = 160$ and 250 GeV are shown in Figure 4.7 and 4.8. Here the t_β dependence and differences between 2HDMs of type I and II are evident. All constraints on the scalars and mixing angles derived in the previous sections are considered.
We consider a value for the dark matter relic density to be reasonable, if it lies between 0.3 and 1.1 times the actual value $(\Omega_\chi h^2)^{Planck} = 0.1198 \pm 0.0015$, measured by the Planck satellite with very high precision [5]. This is justified because we do not demand that χ is the only, but just a significant component of the dark matter abundance.
First, we sketch the derivation of the annihilation cross section for our main dark matter annihilation channel for a better understanding of the numerical results presented in the following. The annihilation cross section is directly connected to the relic density as shown in Section 1.3.

4.7.1 Calculation of the Annihilation Cross Section

The main annihilation channel for the dark matter is $\chi\bar{\chi} \to A \to b\bar{b}$, the corresponding Feynman diagram is shown in Figure 4.5 [51]. In the following we derive the cross section of this process at first order to get a better understanding of the relic density distributions shown below.
The tree-level matrix element for this process reads [15, 58]

$$\mathcal{M} \;=\; \bar{v}_s(p')\, g_{A5}\, \gamma_5\, u_{s'}(p)\, \frac{i}{q_A^2 - M_A^2 - iM_A\Gamma_A}\, \bar{u}_r(k)\, \frac{\kappa_{Ad}\, m_b}{v}\, \gamma_5\, v_{r'}(k')\,, \qquad (4.7)$$

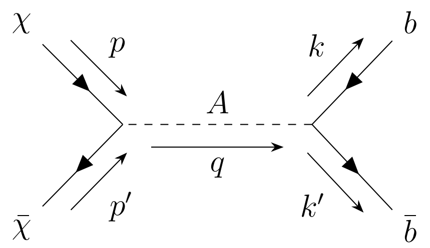

Figure 4.5: Feynman diagram for the process $\chi\bar{\chi} \to A \to b\bar{b}$, which is the most important annihilation channel for the relic density. Drawn with [51].

where Γ_A is the total decay width of A calculated from the partial widths in Eq. (3.32) to (3.35). For further calculations, the following trace identity for averaging over the spins will be helpful

$$\begin{aligned}\sum_{s,s'} \bar{v}_{s'}(p')\gamma_5 u_s(p)\, \bar{u}_s(p)\gamma_5 v_{s'}(p') &= \mathrm{Tr}\left[(\not{p}' - m_\chi)\gamma_5(\not{p} + m_\chi)\gamma_5\right] \\ &= -4\left(pp' + m_\chi^2\right) = -2\,(p+p')^2 \,. \end{aligned} \tag{4.8}$$

The spin-averaged squared matrix element, using the result in Eq. (4.8), is given by

$$\begin{aligned}\sum_{s,s',r,r'} |\mathcal{M}|^2 &= g_{A5}^2 \left(\frac{\kappa_{Ad}\, m_b}{v}\right)^2 \frac{1}{\left|q_A^2 - M_A^2 - iM_A\Gamma_A\right|^2} \\ &\quad \sum_{s,s',r,r'} \left(\bar{v}_{s'}(p')\gamma_5 u_s(p)\, \bar{u}_r(k)\gamma_5 v_{r'}(k')\right)\left(\bar{u}_s(p)\gamma_5 v_{s'}(p')\, \bar{v}_{r'}(k')\gamma_5 u_r(k)\right) \\ &= 4\, g_{A5}^2 \left(\frac{\kappa_{Ad}\, m_b}{v}\right)^2 \frac{(p+p')^2\,(k+k')^2}{\left(q_A^2 - M_A^2\right)^2 + M_A^2\,\Gamma_A^2} \,. \end{aligned} \tag{4.9}$$

For the overall cross section one has to sum over the color charges, which leads to an additional color factor $N_c = 3$ only for the quarks in the final state, as χ does not carry a color charge. The annihilation cross section reads

$$\begin{aligned}\sigma_{ann} &= \frac{1}{16\pi s}\sqrt{\frac{1-4m_b^2/s}{1-4m_\chi^2/s}} \sum_{spins,color} |\mathcal{M}|^2 \\ &= \frac{N_c}{4\pi}\sqrt{\frac{s-4m_b^2}{s-4m_\chi^2}} \left(\frac{g_{A5}\,\kappa_{Ad}\, m_b}{v}\right)^2 \frac{s}{\left(s-M_A^2\right)^2 + M_A^2\,\Gamma_A^2} \,, \end{aligned} \tag{4.10}$$

where we have introduced the Mandelstam variable $s = (p+p')^2 = (k+k')^2$.
For the relic density the thermally averaged annihilation cross section $\langle\sigma_{ann} v\rangle$ is needed. In the non-relativistic limit, where $s = 4m_\chi^2$ and $v = \sqrt{\frac{s}{m_\chi^2} - 4}$, it is in good approxi-

mation given by

$$\langle \sigma_{ann} v \rangle \;\approx\; \sigma_{ann}\, v \;=\; \frac{N_c}{4\pi}\, \frac{\sqrt{s - 4m_b^2}}{m_\chi}\, \left(\frac{g_{A5}\, \kappa_{Ad}\, m_b}{v}\right)^2 \frac{4m_\chi^2}{\left(4m_\chi^2 - M_A^2\right)^2 + M_A^2\,\Gamma_A^2}\,. \tag{4.11}$$

It is easy to see that $\langle \sigma_{ann} v \rangle$ has a maximum for $m_\chi = M_A/2$ and therefore, the relic density is minimal around this point, called (pseudoscalar-) pole. A similar result can be obtained by taking h as the mediator, leading to a minimum of $\Omega_\chi h^2$ around $m_\chi \simeq m_h/2$.

4.7.2 Results and discussion

In this section the numerical results calculated with micrOmegas version 4.3.1 [20, 21], based on a CH output written with FeynRules version 2.3.24 [54, 55], are presented for $M_H = M_{H^\pm} = 500$ GeV and $c_{\beta-\alpha} = 0$ as derived above.
Figure 4.6 shows contours of constant relic densities in the m_χ-C_5 plane with $M_A = 160$ GeV (left) and $M_A = 250$ GeV (right), and $t_\beta = 1$, and the results are valid for 2HDMs of type I and II. The dominant structure is the pseudoscalar pole at $m_\chi \lesssim M_A/2$, where the annihilation is very efficient as shown above, and therefore, the coupling has to be very small to get reasonable values of $\Omega_\chi h^2$, which are drawn in green. For the mono-X searches at the LHC, discussed in the next section, A should be able to decay on-shell into $\bar{\chi}\chi$, therefore values of $m_\chi \leq M_A/2$ are preferred. In this mass region no fine tuning is needed, as C_5 can be chosen between roughly 0.25 and 2.5.
After the order of magnitude of C_5 is fixed, we look at the t_β dependence and differences between the two types of 2HDMs. Figure 4.7 shows the relic density in the $m_\chi - t_\beta$ plane for $M_A = 160$ GeV (left) and $M_A = 250$ GeV (right) with $\mathrm{Re}(C_5) = 0.37$, or $\frac{\mathrm{Re}(c_5)}{\Lambda} = 1.5 \times 10^{-3}$ GeV^{-1}, respectively, and all other couplings equal to zero in a 2HDM of type I. The corresponding plot for a 2HDM of type II is shown in Figure 4.8. The regions of reasonable values of $\Omega_\chi h^2$ are marked in green and form two bands, one for $m_\chi < M_A/2$ and another one for $m_\chi > M_A/2$. As said above, the first region is preferred. The red shaded area marks $m_\chi < M_h/2$, which is disfavored from Higgs measurements. For both types the relic density is small near the pseudoscalar pole $m_\chi = M_A/2$, because the annihilation is very efficient as calculated above.
In both types the main decay of A is to $b\bar{b}$ below the top threshold, and therefore the t_β-dependence is inverted between 2HDM of type I and II. In models of type I values of $t_\beta < 1$ are favored, which are excluded by other experiments. The plot shows a very narrow band of reasonable values around the pseudoscalar pole for $t_\beta > 1$. A 2HDM of type II is preferred as is leads to wide regions with reasonable values of $\Omega_\chi h^2$ for $t_\beta \gtrsim 1$. The relic density also favors $t_\beta < 10$ like other constraints and shows no (visible) dependents on $c_{\beta-\alpha}$, because the pseudoscalar couplings only dependent on t_β.

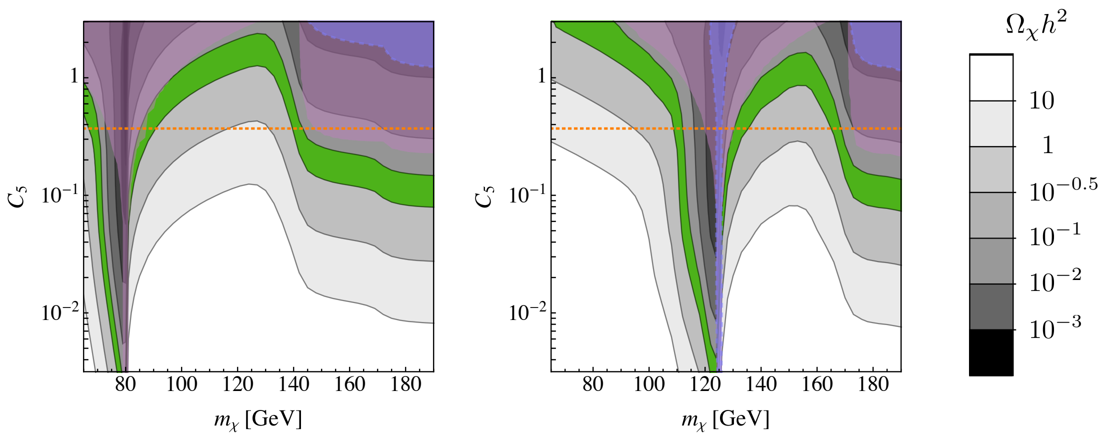

Figure 4.6: Relic density for $M_A = 160$ GeV (left) and $M_A = 250$ GeV (right), $t_\beta = 1$, in dependence of Re(C_5) and m_χ. All other couplings are zero and $M_H = M_{H^\pm} = 500$ GeV and $c_{\beta-\alpha} = 0$. The green band marks values of $\Omega_\chi h^2$ between 0.04 and 0.13. At the pole very small couplings are needed because of the efficient annihilation there.
The light purple region is excluded from the CMB bounds and the dark purple region from the proposed CTA results.

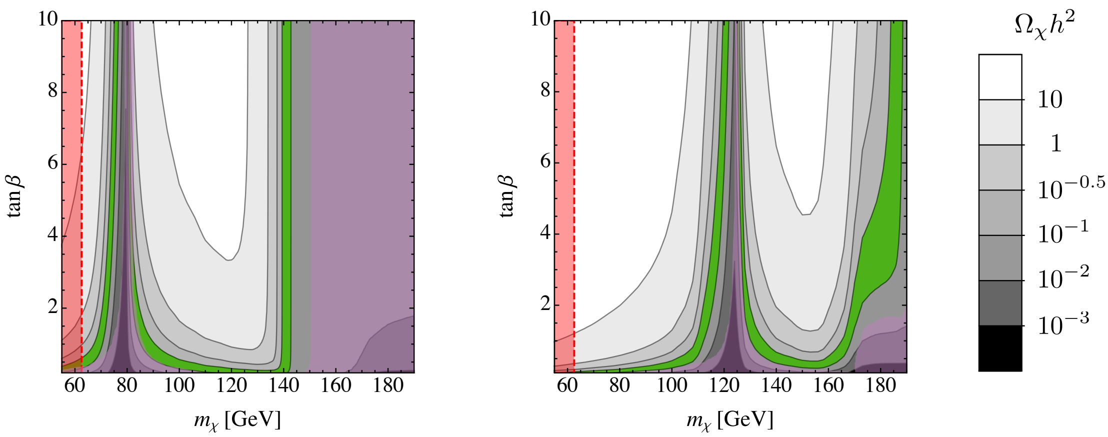

Figure 4.7: Relic density for $M_A = 160$ GeV (left) and $M_A = 250$ GeV (right) with Re$(C_5) = 0.37$ and all other couplings equal to zero, $M_H = M_{H^\pm} = 500$ GeV and $c_{\beta-\alpha} = 0$ in a 2HDM of type I. The green band marks values of $\Omega_\chi h^2$ between 0.04 and 0.13.
The red shaded area for $m_\chi < M_h$ is disfavored from Higgs physics, see 4.1.
The light purple region is excluded from the CMB bounds and the dark purple region from the proposed CTA results.

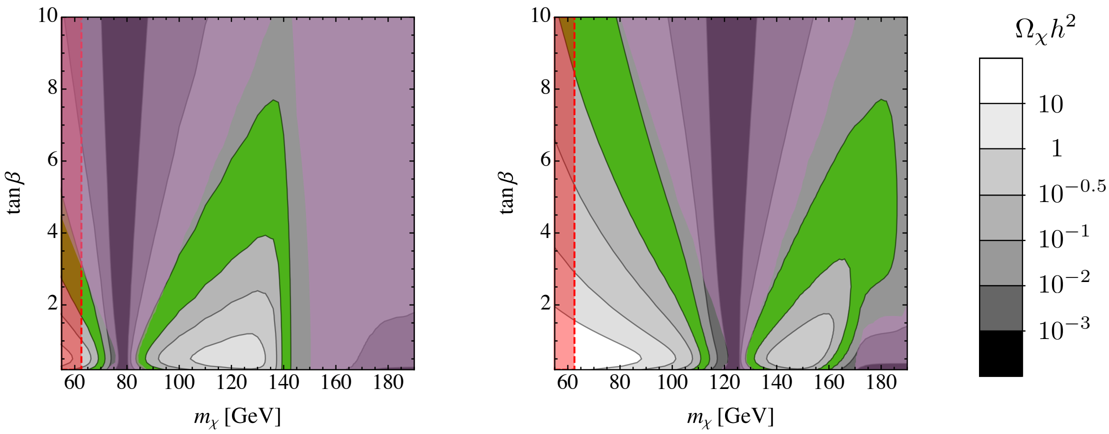

Figure 4.8: Relic density for $M_A = 160$ GeV (left) and $M_A = 250$ GeV (right) with Re$(C_5) = 0.37$ and all other couplings equal to zero, $M_H = M_{H^\pm} = 500$ GeV and $c_{\beta-\alpha} = 0$ in a 2HDM of type II. The green band marks values of $\Omega_\chi h^2$ between 0.04 and 0.13.
The red shaded area for $m_\chi < M_h$ is disfavored from Higgs physics, see 4.1.
The light purple region is excluded from the CMB bounds and the dark purple region from the proposed CTA results.

Even though we concentrate on $m_\chi < M_A/2$ for the collider searches, we shortly explain the behavior of $\Omega_\chi h^2$ for higher dark matter masses. At $m_\chi \approx \frac{m_A+m_h}{2}$ the decay channel $\chi\bar{\chi} \to hA$ opens and the total annihilation cross section increases again and therefore the relic density goes down. Above $m_\chi \approx m_t$, the momentum transfer is high enough to enable the pseudoscalar A to decay to an on-shell top quark pair. Opening this decay channel increases the cross section significantly and causes a sharp descend in the relic density. It depends on the mediator mass which channel opens first, for $M_A \lesssim 215$ GeV it is $\chi\bar{\chi} \to hA$ and for higher masses it is $\chi\bar{\chi} \to t\bar{t}$, which can be seen in the plots for $M_A = 160$ GeV and $M_A = 250$ GeV in Figure 4.7 and 4.8. They can be distinguished as the coupling to hA has no t_β-dependence. This is valid for 2HDMS of type I and type II. Both effects explain that the relic density reaches reasonable and even smaller values for high m_χ.

In all cases we find sets of parameters which result in reasonable value for the relic density without the need of fine tuning. Or the other way around, if M_A, C_χ and C_5 are fixed, wide regions of m_χ and t_β are disfavored.

We shortly discuss the effect of varying the different parameters in a 2HDM of type II. Always one parameter is changed at a time and the described effects add up.

Changing the value of M_A shifts the region of reasonable values of $\Omega_\chi h^2$ to values around $m_\chi = M_A/2$, as shown in Figures 4.7 and 4.8. Increasing Re(C_5) moves the left (right) band slightly to the left (right) and broadens it. Decreasing it leads to the opposite effect. Setting Im$(C_\chi) \approx$ Re(C_5) and therefore allowing for a CP violating

coupling of A to χ has no visible effect on the relic density. Choosing it significantly higher, broadens and flattens the band of reasonable values but does not change the structure.
Adding a coupling to h by setting $\mathrm{Re}(C_\chi) \approx 1.1 \times 10^{-2}$ (the highest value allowed by direct detection experiments) leads to an additional Higgs pole, a small vertical band with a reasonable density at $m_\chi \approx m_h/2$, and a smooth transition to the former distribution. For much higher values of $\mathrm{Re}(C_\chi)$, ignoring the direct detection bounds for a moment, m_χ would get a significant contribution from the Higgs mechanism, see Eq. (3.5). This leads to a t_β dependence of m_χ and distorts the distribution.
The last coupling parameter $\mathrm{Im}(C_5)$ again breaks CP and is more complicated, because it generates a complex mass term. To prevent this, it is necessary to perform a chiral rotation and field redefinition as described in Section 3.2 and to use $m_{\chi,rot}$, given in Eq. (3.10), instead of m_χ. The chiral rotation also induces a value for $\mathrm{Re}(C_\chi^{rot})$. The direct detection exclusion limits lead to $\mathrm{Im}(C_5) < 3.7 \times 10^{-2}$ for $\mathrm{Re}(C_\chi) = 0$, or $\frac{\mathrm{Im}(c_5)}{\Lambda} < \frac{1.5}{10^4 \mathrm{GeV}}$. The Higgs pole is wider than in the case above, it covers $m_\chi \approx 58 - 62$ GeV, while the rest is nearly unchanged. For higher values, again ignoring direct detection bounds, the whole plot is distorted.

4.7.3 Further Operators

Our calculations for direct detection experiments allow for a maximum value for all three couplings of $\approx 1.5 \times 10^{-5} \frac{1}{\mathrm{GeV}}$, which corresponds to $\mathrm{Re}(C_\chi) \lesssim 3.7 \times 10^{-4}$.
The influence on the relic density distribution is similar to choosing higher values of $\mathrm{Re}(c_\chi)$, so the extra operators do not give rise to new phenomena. Just the Higgs-pole has a slightly different shape. Therefore it is reasonable to skip a more detailed discussion.

4.7.4 Higher Order Insertions

As shown in Figure 4.9 for a pure pseudoscalar mediator with $M_A = 160$ GeV, where only $\mathrm{Re}(c_5)$ is unequal to zero, the band of reasonable values for the relic density is nearly vertical for $t_\beta > 3$ in the $n = 2$ case, in contrast to the band for a single insertion of $H_1^\dagger H_2$.

4.8 Indirect Detection

As mentioned in the introduction, indirect detection experiments search for effects of dark matter annihilation processes on different observables. For example this could be done by searching for annihilation remnants or the effects on the CMB.
We consider constraints on the total dark matter annihilation cross section, which are derived from CMB measurements and the new Cherenkov Telescope Array (CTA). To

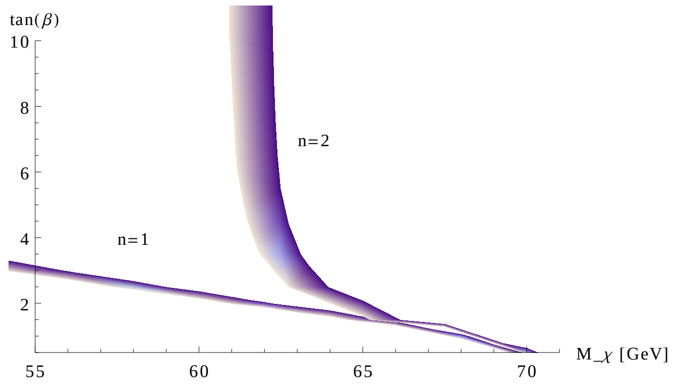

Figure 4.9: Bands for Ωh^2 between 0.1 and 0.12 for the $n = 1$ and $n = 2$ cases, where only Re(c_5) is unequal to zero, but the actual values are not compatible because of the different scaling, and $M_A = 160$ GeV. Darker regions have lower values of $\Omega_\chi h^2$.

avoid a significant reheating of the CMB, the effective annihilation cross section of dark matter to photons at the time of decoupling has to be small. The resulting bound is [5, 28]

$$f_{eff}\,\frac{(\sigma v)_{ann}}{m_\chi} \lesssim 3\,\times 10^{-28}\frac{\text{cm}^3}{\text{s GeV}}\,, \tag{4.12}$$

where $f_{eff} = 0.35$ for b-quarks being the main annihilation product [27] and $(\sigma v)_{ann}$ is the annihilation cross section at decoupling. As the velocity averaged annihilation cross section is (nearly) independent of the mean velocity v in our model and the velocity is the main quantity that changes during the expansion, we approximate $(\sigma v)_{ann}$ with the annihilation cross section today calculated by micrOmegas.

Second, we consider the expected bounds of CTA shown in Figure 4.10 [26]. Again we use the annihilation cross section calculated by micrOmegas. After matching our parameters to the coefficients of the simplified model with a pseudoscalar mediator and Dirac dark matter used in [26], we were able to reproduce the curves for the cross section, shown in the upper right corner of Figure 4.10, for $m_\chi \lesssim M_A/2$. For higher dark matter masses $\Gamma(\chi\bar{\chi} \to hA)$ gets important, which is not accessible in their model and increases our annihilation cross section. In addition we have a dependence on t_β with a minimum around one, therefore very small or large values of t_β can be excluded.

Both constraints are plotted in Figures 4.7 and 4.8 together with the relic density. The region excluded by CTA (CMB) is drawn in dark (light) purple. The CMB measurements lead to constraints roughly one order of magnitude stronger than the proposed CTA results. The CMB bound excludes parameter points where the annihilation cross section is large and the relic density is much smaller than the actual value. Therefore, regions disfavored by the relic density calculations can be excluded.

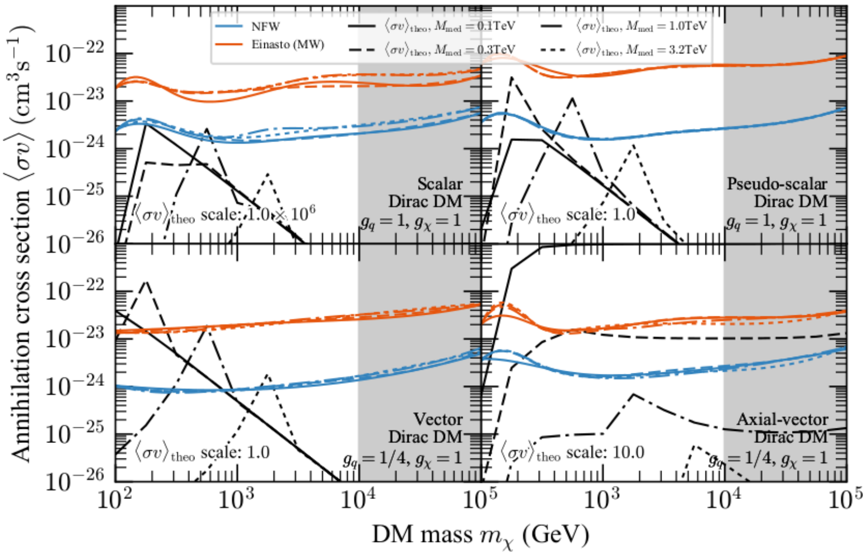

Figure 4.10: Excluded annihilation cross sections for different simplified models projected by the CTA experiment. Limits are shown for two considered dark matter density profiles (blue and orange lines) and for different mediator masses $M_{med} = M_A = 0.1, 0.3, 1,$ and 3.2 TeV. The theoretical cross sections, shown in black and upscaled by a factor of 10^6 and 10 for the scalar and axial-vector dark matter, respectively, have been reproduced for the pseudoscalar case. The gray shaded region for $m_\chi > 10$ TeV, indicates that their NLO approximation breaks down. Figure from [26].

ATLAS Mono-Jet	CMS mono-Z	CMS $t\bar{t}$-associated
$E_T^{\text{miss}} > 250$ GeV	$p_T^e > 25/20$ GeV	$E_T^{\text{miss}} > 200$ GeV
$p_T^j > 250$ GeV	$m_Z - 15 < m_{ee} < m_z + 10$ GeV	lepton veto $p_T^l > 10$ GeV
$\lvert\eta_j\rvert < 2.4$	$\lvert\eta_e\rvert < 2.4$	Jets ≥ 4 with $p_T^j > 20$ GeV
lepton veto $p_T^e > 20$ GeV	3rd-lepton veto $p_T^{e,\mu} > 10$ GeV	number b tags ≥ 2
lepton veto $p_T^\mu > 10$ GeV	3rd-lepton veto $p_T^\tau > 18$ GeV	$\Delta\phi\left(\text{jet}, E_T^{\text{miss}}\right) > 1.0$ radians
Jets ≤ 4 with $p_T^j > 30$ GeV	$p_T^{ee} > 60$ GeV	
$\Delta\phi\left(\text{jet}, p_T^{\text{miss}}\right) > 0.4$ radians	Jets ≤ 1 with $p_T^j > 30$ GeV	
	Top quark veto $p_T^b > 20$ GeV	
	$E_T^{\text{miss}} > 100$ GeV	
	$\left\lvert E_T^{\text{miss}} - p_T^{ee}\right\rvert / p_T^{ee} < 0.4$	
	$\Delta\phi\left(ee, \vec{p}_T^{\,\text{miss}}\right) > 2.8$ radians	
	$\Delta\phi\left(\text{jet}, E_T^{\text{miss}}\right) > 0.5$ radians	

Table 4.1: Cuts implemented for the three simulated mono-X searches. Table from [46]

4.9 Mono-X searches

To derive constraints on our model parameters from mono-X searches at the LHC we perform Monte Carlo simulations based on an Universal FeynRules Output (UFO) implementation of the presented simplified model where we use FeynRules 2.3.24 [54, 55] and the NLOCT package [59] embedded in FeynArts 3.9 [60].

4.9.1 Analysis Framework and Cuts

The hard matrix elements are calculated with Madgraph5_aMC@NLO 2.5.5 [61] and the hadron showering is performed with the Pythia 8.226 [62] interface for Madgraph and the fast detector simulation with Delphes 3.4.0 [63]. For details about the implementation, signal generation, and jet merging see [46].
The analyses are executed in the MADANALYSIS5 framework [64] and based on mono-jet searches from ATLAS [65] and mono-Z and $t\bar{t}A$ searches from CMS [66, 67]. We implemented the cuts used in these searches as far it was possible. The cuts are listed in Table 4.1. To test the implementation Standard Model background events are generated, like $Z \to \nu\nu +$ jets for the mono-jet cuts, and they show reasonable agreement with the measurements [46]. The cuts are explained in more detail in [46, 65, 66, 67].

4.9.2 Discussion of Mono-jet

One attempt to detect dark matter is the search for missing transverse energy (MET) accompanied by mono-jets which refers to jets radiated of the initial state. An example

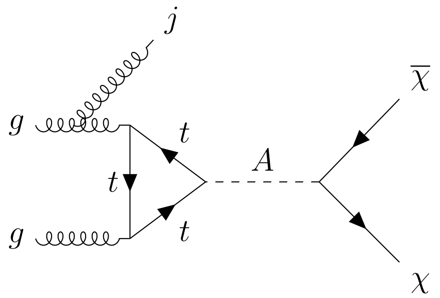

Figure 4.11: Example of a Feynman-diagram for mono-jets production. Drawn with [51].

for such processes is given in Figure 4.11.
For the signal generation we use Madgraph5_aMC@NLO where we require one jet radiated of the initial state next to the production of a gluon loop induced pseudoscalar decaying into a pair of dark matter fermions. This jet is allowed to emerge either from the hard matrix element directly or from the showering process performed with Pythia. The dark matter particles provide the missing transverse energy we require to consider the event as a signal.
With the current data set of 36.1 fb^{-1} values of t_β below 0.5 can be excluded up to a pseudoscalar mediator mass of 340 GeV, cf. Figure 4.14. The sharp cut-off can be explained by the opening of the top-decay channel where the pseudoscalar dominantly decays into a pair of top quarks, see the left plot of figure 3.2.
In Figure 4.15 the exclusion limits for the mono-X searches are presented in the $c_{\beta-\alpha}$-t_β plane for pseudoscalar masses of 160 GeV (left) and 250 GeV (right). In the right panel the decay $A \to hZ$ becomes present for $c_{\beta-\alpha} \neq 0$, so the bounds become slightly weaker towards the edges due to this decay. In the setting of the left panel the pseudoscalar is lighter than $m_h + M_Z$ and this decay is kinematically forbidden. As the uncertainty of the Standard Model prediction for the total number of events in the inclusive signal region is mainly restricted by systematic uncertainties, the reach of this study for higher luminosity is limited by those. So higher statistics only slightly improves the exclusion bounds of this search channel [46].

4.9.3 Discussion of Mono-Z

As mentioned in the introduction initial state radiation of Z bosons is almost negligible compared to the production of mono-jets as it is suppressed by the weak coupling as well as its mass, cf. Figure 1.6. However, in our model a resonant enhanced process exists, as the heavy scalar H can decay into A and Z, see Figure 4.12.
In our analysis H is generated via a top-loop, since for small values for t_β the contribution of the lighter quarks give only A small correction to the total production cross section, but enhance the calculation time. We require the Z boson to decay into a pair of electrons whereas A should decay into dark matter. It should be stressed

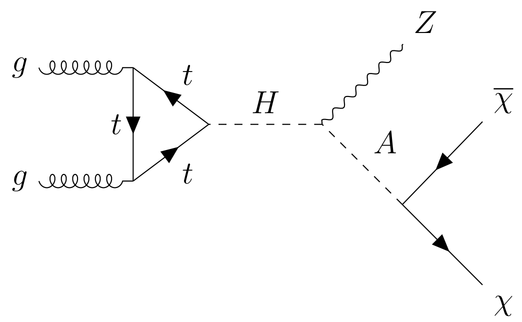

Figure 4.12: Feynman-diagram for the resonant mono-Z production via the heavy scalar H. Drawn with [51].

that the BR($H \to AZ$) dominates over BR($H \to AA$) in the considered region of $t_\beta \approx \mathcal{O}(1)$. This is remarkably, as for pseudoscalar masses below 250 GeV the latter branching ratio dominates away from $t_\beta = 1$, cf. Figure 3.1. One could expect that for $M_A > 250$ GeV a bump in the mono-Z spectrum in Figure 4.14 occur as the branching ratio BR($H \to AZ$) suddenly increases. With the current study we can exclude values up to $t_\beta \approx 1.2$at this transition point as can be seen in Figure 4.14. However, close to $t_\beta = 1$ the decay $H \to AA$ contributes only about 2% to the total width and therefore no distinct increase can be seen.
For pseudoscalars with $M_A \lesssim 250$ GeV values for t_β up to 1.5 can be excluded. For increasing M_A sensitivity is dropping as an H with a mass of 500 GeV tends to decay more likely into a pair of top quarks. Sensitivity is finally completely lost at $M_A \approx 340$ GeV where the decay of A into a top quark pair becomes available. In Figure 4.15 the dependence of the signal strength on t_β and $c_{\beta-\alpha}$ is shown. In the left panel M_A is set to 160 GeV. The strongest bounds of the mono-Z are obtained in the alignment limit as BR($H \to AZ$) is maximal whereas it vanishes for $c_{\beta-\alpha} = \pm 1$. In the right panel of Figure 4.15 the behavior changes slightly as for $M_A = 250$ GeV the pseudoscalar is heavy enough to open the channel $A \to hZ$, which reduces the signal strength away from the alignment limit.
Statistical uncertainties of the signal generation and the analysis are $\approx 1 - 2\%$ and therefore rather small compared to the ones of the mono-jet study. The scale variation for the leading order is approximately 20% and expected to be significantly smaller at NLO. PDF uncertainties are about 4.9% [46].
We expect that this search at 12.9 fb^{-1} is not yet at its full potential and slightly stronger limits from the high luminosity run at the LHC can be expected.

4.9.4 Discussion of $t\bar{t}A$ Production

Heavy quark associated production of dark matter also has the potential to provide dark matter signatures at colliders. As we implement our model as a 2HDM of type II only

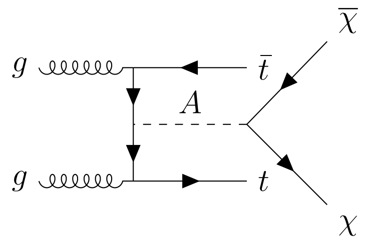

Figure 4.13: Feynman-diagram $t\bar{t}$ - associated production. Drawn with [51].

the top quark production provides relevant contributions for small t_β. An advantage of the associated production compared to the two searches discussed above is that the production of dark matter is an interaction at tree-level, whereas the processes discussed above are loop suppressed. On the other side getting two top quarks out of a hadron is costly and works mainly via gluon-splitting, cf. Figure 4.13 [46].

The events are generated at leading order and along with the analysis have a statistical uncertainty of about 10%. The PDFs have a uncertainty of 8.1% and the scaling at leading order contributes about 25%, but is expected to decrease considering NLO corrections.

The search is most sensitive for low M_A as the pseudoscalar needs to be produced and does not emerge from a resonant decay. As soon as the top-threshold for the pseudoscalar is reached sensitivity is lost. This channel is comparable to the mono-jets signal and excludes $t_\beta < 0.5$ for most of the mediator masses. As shown in Figure 4.15, for a light mediator of 160 GeV this process is independent of $c_{\beta-\alpha}$ whereas for 250 GeV the bounds get slightly weaker for increasing $c_{\beta-\alpha}$ as the channel $A \to hZ$ becomes available 4.15. This search at 2.2 fb^{-1} is limited at the current state mostly by statistics and expected to reveal its full potential at the HL-LHC.

4.9.5 Final Plots

The gray region in both panels of Figure 4.15 is obtained by the combination of constraints on the scalar sector derived in the previous sections. Here we assume our model to be complete in the sense that all new physics we integrated out is to heavy or weakly coupled to effect the derived conditions on the parameters related to the spin 0 particles. This has not to be the case as new charged particles could for example relax the flavor bounds significantly. A further breaking of the assumed symmetry (or completely ignoring it) would allow for additional quartic couplings in the scalar potential. This would weaken the stability requirements, especially on t_β as shown in the right panel of Figure 4.4. Therefore, the gray region is not necessarily forbidden, but it is interesting to see that even the minimal approach is not completely excluded.

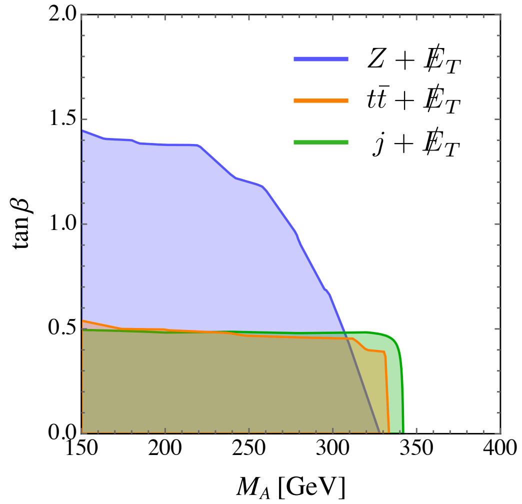

Figure 4.14: Regions in the $M_A - t_\beta$ plane excluded by mono-Z (blue) and mono-jet searches (green), and $t\bar{t}A$ production (red) for $c_{\beta-\alpha} = 0$ and $M_H = 500$ GeV. Figure from [46].

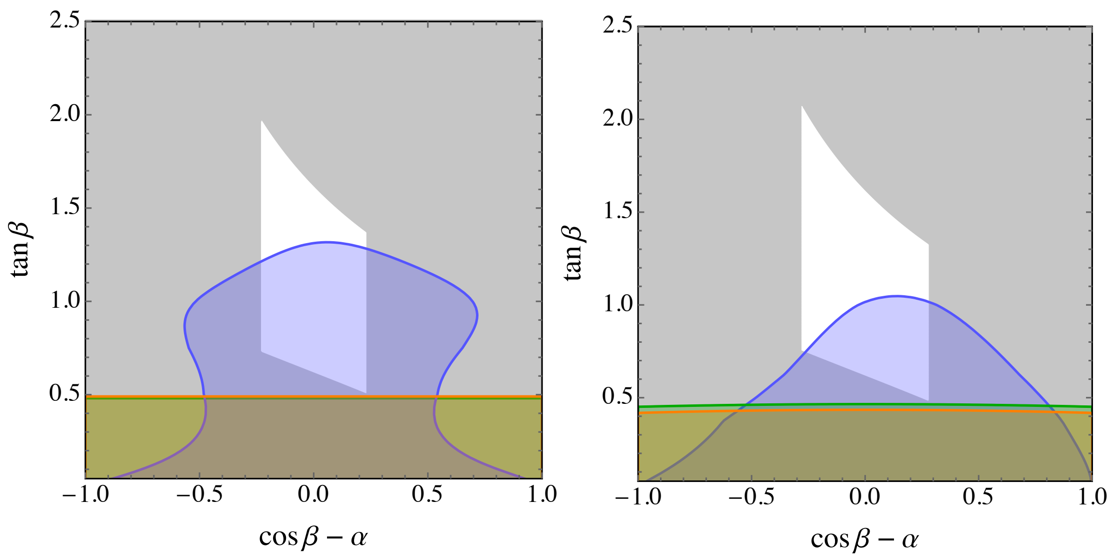

Figure 4.15: Regions in the $c_{\beta-\alpha} - t_\beta$ plane for $M_A = 160$ GeV (left) and 250 GeV (right) excluded by mono-Z (blue), mono-jet searches (green), and $t\bar{t}A$ production (red). The gray region is excluded from a combination of flavor and stability requirements. Figure from [46].

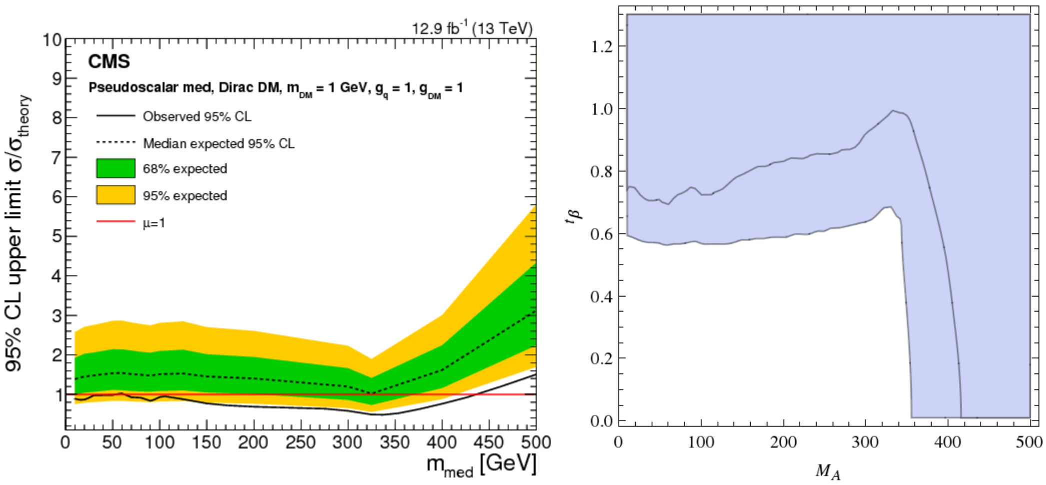

Figure 4.16: Left: Expected (dotted black line) and observed (solid black line) 95% C.L. upper limits on the signal strength μ as a function of the pseudoscalar mediator mass from the monojet signal process. Figure from [69].
Right: Excluded regions in our parameter space. The white region is obtained by considering the expected curve of the left figure and the black line by considering the observation at 95% C.L.

4.9.6 Mono-Jet Bound from Theory

To validate the mono-jet simulations, we calculated the exclusion bounds in our parameter space directly from the data in the left panel of Figure 4.16 [68, 69].

This is possible since in the case of mono-jet searches the simplified model with a pseudoscalar mediator, used in this paper, leads to the same phenomenology up to a universal rescaling of the coupling strength of the pseudoscalar A to top quarks, which changes from $g_q = 1$ to $g_{Att}\frac{m_t}{vt_\beta}$. An easy rescaling allows for interpreting the results as exclusion limits for t_β. The branching ratios of A, dominantly decaying into dark matter, are also more complicated in our model, since A can decay to all quarks and leptons with a t_β-depending coupling instead of decaying only to tops with a constant coupling[3]. Note that the influence is not strong because the dominant decays are the same in both cases, nevertheless we corrected the cross section with the ratio of the two branching ratios of the dark matter decay.

The resulting exclusion line is comparatively strong. It reaches $t_\beta = 1$, see right panel of Figure 4.16, and into the region of the mono-Z bounds and clearly above the ATLAS results and the ones obtained from our Monte Carlo simulations. For masses $M_A > 2m_t$ effectively no values of t_β can be excluded because A mainly decays into a top quark pair. For $M_A < 2m_\chi$ there are of course no exclusion limits, as A cannot to decay into

[3] We do not take off-shell effects into account.

dark matter.
The better results compared to ATLAS could be due to the fact that the analysis is optimized for a pseudoscalar decaying exclusively to dark matter (under the top threshold) in the considered mass regime and a bit more aggressive cuts.

5 Conclusion

We study the universal properties of pseudoscalar mediators for dark matter based on a consistent gauge-invariant simplified model with a second $SU(2)_L$ doublet and effective dimension five couplings to the dark sector. This approach has an assessable parameter space and covers a wide class of models with pseudoscalars mediators, which are a promising candidate for searches at the LHC.

We showed that a general feature of such models is a resonantly enhanced mono-Z signal, which leads to the dominant exclusion bounds from collider searches in a wide range of the preferred parameter space.

We like to emphasize that there are good reasons to look for resonantly enhanced mono-Z signals. This could clearly improve the exclusion bounds compared to the analysis of Z-radiation from initial state. It has been shown that for initial state radiation mono-jet signals give much stronger bounds but the resonantly enhanced production of mono-Z signals in our model can break this hierarchy.

The scalar sector is constraint by measurements of the Higgs couplings, flavor changing currents, electroweak precision observables, and by collider searches for heavy spin 0 particles. The assumed symmetry forbids many terms of the general 2HDM potential and therefore, stability and unitarity requirements put strong constraints on the remaining parameters, mainly the mixing angles.

For the dark matter part, the relic density is calculated and it is shown that no fine-tuning of the couplings and masses is needed to get values slightly below the measured value. We also take the actual exclusion limits from direct and indirect detection experiments into account and are able to avoid them as pseudoscalar mediators lead to velocity suppressed cross sections in direct detection experiments. All these constraints leave out a compatible small region in the open parameter space and most of this region can be tested in future LHC runs.

If the additional states, which has been integrated out to obtain the effective dark matter operators, are not much heavier than the considered spin 0 particles they could influence and most likely weaken several bounds, especially those from flavor physics and stability requirements. But even if all further particles are much heavier or very weakly coupled to the Standard Model the presented model is valid and could serve as a proper theory for physics around the weak scale. This is not obvious since the bounds taken into account over constrain our model.

Outlook

A natural extension of this model is to use $H_1^\dagger H_2$ as the flavon and expand the proposed

symmetry to the Standard Model quarks, as done in [43]. The additional dark matter couplings and decays could relax the bounds found there and lead to interesting new signatures.
In this thesis only CP conserving couplings are taken into account, it could be interesting to investigate CP violating couplings in the dark sector and see if they might effect the visible sector.
We mentioned two possible UV completions for an extended dark sector. It would be interesting to see how exactly they match to our effective description and if one can find other theories.

Acknowledgments

I want to thank my colleges of the working group for fruitful discussions and a lot of fun in the coffee room, especially Elias for spontaneous proof reading and Martin for nice teamwork during the whole work.
A special thank goes to Martin Bauer for excellent supervision during the last year and to Tilman Plehn for the opportunity to get this insight into the fascinating topic of particle dark matter and helpful advices.

Erklärung:

Ich versichere, dass ich diese Arbeit selbstständig verfasst habe und keine anderen als die angegebenen Quellen und Hilfsmittel benutzt habe.

Heidelberg, den 29.09.2017 . . . .

6 Bibliography

[1] J. H. Oort. “The force exerted by the stellar system in the direction perpendicular to the galactic plane and some related problems”. In: *Bulletin of the Astronomical Institutes of the Netherlands* 6 (Aug. 1932), p. 249.

[2] Matts Roos. “Dark Matter: The evidence from astronomy, astrophysics and cosmology”. In: (2010). arXiv: 1001.0316 [astro-ph.CO].

[3] F. Zwicky. “Die Rotverschiebung von extragalaktischen Nebeln”. In: *Helvetica Physica Acta* 6 (1933), pp. 110–127.

[4] Flip Tanedo. *Defense Against the Dark Arts*. 2011. URL: http://www.physics.uci.edu/~tanedo/files/notes/DMNotes.pdf.

[5] P. A. R. Ade et al. “Planck 2015 results. XIII. Cosmological parameters”. In: *Astron. Astrophys.* 594 (2016), A13. DOI: 10.1051/0004-6361/201525830. arXiv: 1502.01589 [astro-ph.CO].

[6] Shy Genel et al. “Introducing the Illustris Project: the evolution of galaxy populations across cosmic time”. In: *Mon. Not. Roy. Astron. Soc.* 445.1 (2014), pp. 175–200. arXiv: 1405.3749.

[7] Douglas Clowe et al. “A direct empirical proof of the existence of dark matter”. In: *Astrophys. J.* 648 (2006), pp. L109–L113. arXiv: astro-ph/0608407.

[8] N. W. Evans. “Dogs that don’t bark? (The Tale of baryonic dark matter in galaxies)”. In: *Proceedings, 4th International Workshop on The identification of dark matter (IDM 2002)*. 2002, pp. 144–158. arXiv: astro-ph/0211302.

[9] Wayne Hu, Rennan Barkana, and Andrei Gruzinov. “Cold and fuzzy dark matter”. In: *Phys. Rev. Lett.* 85 (2000), pp. 1158–1161. DOI: 10.1103/PhysRevLett.85.1158. arXiv: astro-ph/0003365 [astro-ph].

[10] H. Baer and Xerxes Tata. “Dark matter and the LHC”. In: *Physics at the Large Hadron Collider*. Ed. by Amitava Datta et al. 2009, pp. 179–203. DOI: 10.1007/978-81-8489-295-6_12. arXiv: 0805.1905 [hep-ph]. URL: https://inspirehep.net/record/785654/files/arXiv:0805.1905.pdf.

[11] Mambrini Y. *Histories of Dark Matter in the Universe*. 2.5.2016. URL: http://www.ymambrini.com/My_World/Books_files/CTA%20sensitivity.pdf.

[12] Emily E. Richards et al. "Baryonic distributions in the dark matter halo of NGC 5005". In: *Mon. Not. Roy. Astron. Soc.* 449.4 (2015), pp. 3981–3996. arXiv: 1503.05981.

[13] E. L. Lokas and G. Mamon. "Dark matter distribution in the Coma cluster from galaxy kinematics: breaking the mass-anisotropy degeneracy". In: *Mon. Not. Roy. Astr. Soc. 343* 401 (2003).

[14] N. Aghanim et al. "Planck 2015 results. XI. CMB power spectra, likelihoods, and robustness of parameters". In: *Astron. Astrophys.* 594 (2016), A11. DOI: 10.1051/0004-6361/201526926. arXiv: 1507.02704 [astro-ph.CO].

[15] Tilman Plehn. *Dark Matter from a Particle Theorist's Perspective*. 8.6.2017. arXiv: 1705.01987. URL: www.thphys.uni-heidelberg.de/~plehn.

[16] D.V. Bugg. "MOND: A review". In: *Canadian Journal of Physics* 93 (Feb. 2015), pp. 119–125. arXiv: 1405.1695 [physics.gen-ph].

[17] Marco Taoso, Gianfranco Bertone, and Antonio Masiero. "Dark Matter Candidates: A Ten-Point Test". In: *JCAP* 0803 (2008), p. 022. DOI: 10.1088/1475-7516/2008/03/022. arXiv: 0711.4996 [astro-ph].

[18] Frank Daniel Steffen. "Dark Matter Candidates - Axions, Neutralinos, Gravitinos, and Axinos". In: *Eur. Phys. J.* C59 (2009), pp. 557–588. DOI: 10.1140/epjc/s10052-008-0830-0. arXiv: 0811.3347 [hep-ph].

[19] *An Introduction to Particle Dark Matter*. WORLD SCIENTIFIC (EUROPE), 2017.

[20] G. Belanger et al. "micrOMEGAs: A Tool for dark matter studies". In: *Nuovo Cim.* C033N2 (2010), pp. 111–116. DOI: 10.1393/ncc/i2010-10591-3. arXiv: 1005.4133 [hep-ph].

[21] G. Belanger, F. Boudjema, and A. Pukhov. "micrOMEGAs : a code for the calculation of Dark Matter properties in generic models of particle interaction". In: *The Dark Secrets of the Terascale: Proceedings, TASI 2011, Boulder, Colorado, USA, Jun 6 - Jul 11, 2011*. 2013, pp. 739–790. DOI: 10.1142/9789814390163_0012. arXiv: 1402.0787 [hep-ph]. URL: https://inspirehep.net/record/1280091/files/arXiv:1402.0787.pdf.

[22] Edward W. Kolb and Turner Michael S. *The Early Universe*. Frontiers in Physics, 1990. ISBN: 0-201-11603-3.

[23] Günter Sigl. *Astroparticle Physics: Theory and Phenomenology*. Springer Atlantis Press, 2017. ISBN: 978-94-6239-242-7.

[24] S.M. Carroll. *Spacetime and Geometry: An Introduction to General Relativity*. Addison Wesley, 2004. ISBN: 9780805387322.

[25] Max-Planck-Institut für Kernphysik. *Research: Dark Matter*. [Online; accessed 19-September-2017]. 2017. URL: https://www.mpi-hd.mpg.de/lin/research_DM.en.html.

[26] Csaba Balázs et al. "Sensitivity of the Cherenkov Telescope Array to the detection of a dark matter signal in comparison to direct detection and collider experiments". In: (2017). arXiv: 1706.01505 [astro-ph.HE].

[27] Tracy R. Slatyer, Nikhil Padmanabhan, and Douglas P. Finkbeiner. "CMB Constraints on WIMP Annihilation: Energy Absorption During the Recombination Epoch". In: *Phys. Rev.* D80 (2009), p. 043526. DOI: 10.1103/PhysRevD.80.043526. arXiv: 0906.1197 [astro-ph.CO].

[28] Wolfgang Altmannshofer et al. "Explaining dark matter and B decay anomalies with an $L_\mu - L_\tau$ model". In: *JHEP* 12 (2016), p. 106. DOI: 10.1007/JHEP12(2016)106. arXiv: 1609.04026 [hep-ph].

[29] E. Aprile et al. "The XENON1T Dark Matter Experiment". In: (2017). arXiv: 1708.07051 [astro-ph.IM].

[30] E. Aprile et al. "First Dark Matter Search Results from the XENON1T Experiment". In: (2017). arXiv: 1705.06655 [astro-ph.CO].

[31] "Dark Matter Summary Plots from CMS for ICHEP 2016". In: (Aug. 2016). URL: https://cds.cern.ch/record/2208044.

[32] Martin Bauer et al. "Validity of dark matter effective theory". In: *Phys. Rev.* D95.7 (2017), p. 075036. DOI: 10.1103/PhysRevD.95.075036. arXiv: 1611.09908 [hep-ph].

[33] Prateek Agrawal et al. "A Classification of Dark Matter Candidates with Primarily Spin-Dependent Interactions with Matter". In: (2010). arXiv: 1003.1912 [hep-ph].

[34] Jason Kumar and Danny Marfatia. "Matrix element analyses of dark matter scattering and annihilation". In: *Phys. Rev.* D88.1 (2013), p. 014035. DOI: 10.1103/PhysRevD.88.014035. arXiv: 1305.1611 [hep-ph].

[35] C. Patrignani et al. "Review of Particle Physics". In: *Chin. Phys.* C40.10 (2016), p. 100001. DOI: 10.1088/1674-1137/40/10/100001.

[36] John F. Gunion and Howard E. Haber. "The CP-conserving two-Higgs-doublet model: the approach to the decoupling limit". In: *Phys. Rev. D* 67 (7 Apr. 2003), p. 075019. DOI: 10.1103/PhysRevD.67.075019. arXiv: 0207010v5.

[37] Jeremy Bernon et al. "Scrutinizing the alignment limit in two-Higgs-doublet models. II. $m_H = 125$ GeV". In: *Phys. Rev. D* 93 (3 Feb. 2016), p. 035027. DOI: 10.1103/PhysRevD.93.035027. arXiv: 1511.03682v2.

[38] Marcela Carena et al. “Impersonating the Standard Model Higgs Boson: Alignment without Decoupling”. In: *JHEP* 04 (2014), p. 015. DOI: 10.1007/JHEP04(2014)015. arXiv: 1310.2248 [hep-ph].

[39] G.C. Branco et al. “Theory and phenomenology of two-Higgs-doublet models”. In: *Physics Reports* 516.1,2 (2012), pp. 1–102. ISSN: 0370-1573. arXiv: 1106.0034v3.

[40] K. G. Klimenko. “Spontaneous Symmetry Breaking in some Higgs Potentials”. In: *Theor. Math. Phys.* 55 (1983), pp. 342–349. DOI: 10.1007/BF01019020.

[41] M. Maniatis et al. “Stability and symmetry breaking in the general two-Higgs-doublet model”. In: *Eur. Phys. J.* C48 (2006), pp. 805–823. DOI: 10.1140/epjc/s10052-006-0016-6. arXiv: hep-ph/0605184 [hep-ph].

[42] Mayumi Aoki et al. “Models of Yukawa interaction in the two Higgs doublet model, and their collider phenomenology”. In: *Phys. Rev. D* 80 (1 July 2009), p. 015017. DOI: 10.1103/PhysRevD.80.015017. arXiv: 0902.4665v3.

[43] Martin Bauer, Marcela Carena, and Katrin Gemmler. “Flavor from the Electroweak Scale”. In: *FERMILAB-PUB-15-251-T, EFI-15-19* (2015). arXiv: 1506.01719v1.

[44] Martin Bauer, Ulrich Haisch, and Felix Kahlhoefer. “Simplified dark matter models with two Higgs doublets: I. Pseudoscalar mediators”. In: *JHEP* 05 (2017), p. 138. DOI: 10.1007/JHEP05(2017)138. arXiv: 1701.07427 [hep-ph].

[45] Michael A. Fedderke et al. “The fermionic dark matter Higgs portal: an effective field theory approach”. In: *Journal of High Energy Physics* 2014.8 (2014), p. 122. arXiv: 1404.2283.

[46] Martin Bauer, Martin Klassen, and Valentin T. Tenorth. “Universal Properties of Pseudoscalar Mediator Models – PRELIMINARY”. In: (). arXiv: 1710.XXXX.

[47] The ATLAS and CMS Collaborations. “Measurements of the Higgs boson production and decay rates and constraints on its couplings from a combined ATLAS and CMS analysis of the LHC pp collision data at $\sqrt{s} = 7$ and 8 TeV”. In: *JHEP08(2016)045* (2016). arXiv: 1606.02266v2.

[48] Georges Aad et al. “Constraints on new phenomena via Higgs boson couplings and invisible decays with the ATLAS detector”. In: *JHEP* 11 (2015), p. 206. DOI: 10.1007/JHEP11(2015)206. arXiv: 1509.00672 [hep-ex].

[49] Vardan Khachatryan et al. “Searches for invisible decays of the Higgs boson in pp collisions at sqrt(s) = 7, 8, and 13 TeV”. In: *JHEP* 02 (2017), p. 135. DOI: 10.1007/JHEP02(2017)135. arXiv: 1610.09218 [hep-ex].

[50] M. Misiak et al. “Updated NNLO QCD predictions for the weak radiative B-meson decays”. In: *Phys. Rev. Lett.* 114.22 (2015), p. 221801. DOI: 10.1103/PhysRevLett.114.221801. arXiv: 1503.01789 [hep-ph].

[51] Joshua Ellis. “TikZ-Feynman: Feynman diagrams with TikZ”. In: *Comput. Phys. Commun.* 210 (2017), pp. 103–123. DOI: 10.1016/j.cpc.2016.08.019. arXiv: 1601.05437 [hep-ph].

[52] Howard E. Haber and Alex Pomarol. “Constraints from global symmetries on radiative corrections to the Higgs sector”. In: *Physics Letters B* 302.4 (1993), pp. 435–441. ISSN: 0370-2693. DOI: https://doi.org/10.1016/0370-2693(93)90423-F. URL: http://www.sciencedirect.com/science/article/pii/037026939390423F.

[53] I. F. Ginzburg and I. P. Ivanov. “Tree-level unitarity constraints in the most general 2HDM”. In: *Phys. Rev.* D72 (2005), p. 115010. DOI: 10.1103/PhysRevD.72.115010. arXiv: hep-ph/0508020 [hep-ph].

[54] Adam Alloul et al. “FeynRules 2.0 - A complete toolbox for tree-level phenomenology”. In: *Comput. Phys. Commun.* 185 (2014), pp. 2250–2300. DOI: 10.1016/j.cpc.2014.04.012. arXiv: 1310.1921 [hep-ph].

[55] Neil D. Christensen and Claude Duhr. “FeynRules - Feynman rules made easy”. In: *Comput. Phys. Commun.* 180 (2009), pp. 1614–1641. DOI: 10.1016/j.cpc.2009.02.018. arXiv: 0806.4194 [hep-ph].

[56] Jeremy Bernon et al. “Scrutinizing the alignment limit in two-Higgs-doublet models. I. $m_h = 125$ GeV”. In: *Phys. Rev. D* (2015), p. 075004. DOI: 10.1103/PhysRevD.93.035027. arXiv: 1507.00933.

[57] Shinya Kanemura et al. “Higgs coupling constants as a probe of new physics”. In: *Phys. Rev. D* 70 (11 Dec. 2004), p. 115002. DOI: 10.1103/PhysRevD.70.115002. arXiv: hep-ph/0408364. URL: http://link.aps.org/doi/10.1103/PhysRevD.70.115002.

[58] Michael E Peskin and Daniel V Schroeder. *An introduction to quantum field theory*. Boulder, CO: Westview, 1995.

[59] Celine Degrande. “Automatic evaluation of UV and R2 terms for beyond the Standard Model Lagrangians: a proof-of-principle”. In: *Comput. Phys. Commun.* 197 (2015), pp. 239–262. DOI: 10.1016/j.cpc.2015.08.015. arXiv: 1406.3030 [hep-ph].

[60] Thomas Hahn. “Generating Feynman diagrams and amplitudes with FeynArts 3”. In: *Comput. Phys. Commun.* 140 (2001), pp. 418–431. DOI: 10.1016/S0010-4655(01)00290-9. arXiv: hep-ph/0012260 [hep-ph].

[61] J. Alwall et al. “The automated computation of tree-level and next-to-leading order differential cross sections, and their matching to parton shower simulations”. In: *JHEP* 07 (2014), p. 079. DOI: 10.1007/JHEP07(2014)079. arXiv: 1405.0301 [hep-ph].

[62] Torbjörn Sjöstrand et al. “An Introduction to PYTHIA 8.2”. In: *Comput. Phys. Commun.* 191 (2015), pp. 159–177. DOI: 10.1016/j.cpc.2015.01.024. arXiv: 1410.3012 [hep-ph].

[63] J. de Favereau et al. “DELPHES 3, A modular framework for fast simulation of a generic collider experiment”. In: *JHEP* 02 (2014), p. 057. DOI: 10.1007/JHEP02(2014)057. arXiv: 1307.6346 [hep-ex].

[64] Eric Conte, Benjamin Fuks, and Guillaume Serret. “MadAnalysis 5, A User-Friendly Framework for Collider Phenomenology”. In: *Comput. Phys. Commun.* 184 (2013), pp. 222–256. DOI: 10.1016/j.cpc.2012.09.009. arXiv: 1206.1599 [hep-ph].

[65] *Search for dark matter and other new phenomena in events with an energetic jet and large missing transverse momentum using the ATLAS detector*. Tech. rep. ATLAS-CONF-2017-060. Geneva: CERN, July 2017. URL: http://cds.cern.ch/record/2273876.

[66] *Search for dark matter in* $\mathrm{Z} + E_{\mathrm{T}}^{\mathrm{miss}}$ *events using* $12.9\ \mathrm{fb}^{-1}$ *of 2016 data*. Tech. rep. CMS-PAS-EXO-16-038. Geneva: CERN, 2016. URL: https://cds.cern.ch/record/2205763.

[67] Albert M Sirunyan et al. “Search for dark matter produced in association with heavy-flavor quarks in proton-proton collisions at sqrt(s)=13 TeV”. In: (2017). arXiv: 1706.02581 [hep-ex].

[68] Albert M Sirunyan et al. “Search for dark matter produced with an energetic jet or a hadronically decaying W or Z boson at $\sqrt{s} = 13$ TeV”. In: *JHEP* 07 (2017), p. 014. DOI: 10.1007/JHEP07(2017)014. arXiv: 1703.01651 [hep-ex].

[69] CMS Collaboration. “Search for dark matter in final states with an energetic jet, or a hadronically decaying W or Z boson using $12.9\ \mathrm{fb}^{-1}$ of data at $\sqrt{s} = 13$ TeV”. In: (2016).